Time-lapse joint inversion of cross-well DC resistivity and seismic data: A numerical investigation

M. Karaoulis (1), A. Revil (1, 2), J. Zhang (1), and D.D. Werkema (3)

(1) Colorado School of Mines, Dept. of Geophysics, Golden, CO, USA.
(2) ISTerre, CNRS, UMR CNRS 5275, Université de Savoie, 73376 cedex, Le Bourget du Lac, France.
(3) U.S. EPA, ORD, NERL, ESD, CMB, Las Vegas, Nevada, USA .

Short Title: Time-lapse joint inversion

Corresponding author: Andre Revil (arevil@mines.edu)

Email from the co-authors:

Werkema.D@epamail.epa.gov, mkaraoulis@mines.edu; junzhang@mymail.mines.edu

Intended for publication in Geophysics

Abstract. Time-lapse joint inversion of geophysical data is required to image the evolution of oil reservoirs during production and enhanced oil recovery, CO_2 sequestration, geothermal fields during production, and to monitor the evolution of contaminant plumes. Joint inversion schemes reduce space-related artifacts in filtering out noise that is spatially uncorrelated while time lapse inversion algorithms reduce time-related artifacts in filtering out noise that is uncorrelated over time. There are several approaches that are possible to perform the joint inverse problem. In this work, we investigate both the Structural Cross-Gradient (SCG) joint inversion approach and the Cross-Petrophysical (CP) approach, which are both justified for time-lapse problem by petrophysical models. In the first case, the inversion scheme looks for models with structural similarities. In second the case, we use a direct relationship between the geophysical parameters. Time-lapse inversion is performed with an actively time-constrained (ATC) approach. In this approach, the subsurface is defined as a space-time model. All the snapshots are inverted together assuming a regularization of the sequence of snapshots over time. First we show the advantage of combining the SCG or CP inversion approaches and the ATC inversion by using a synthetic problem corresponding to cross-hole seismic and DC-resistivity data and piecewise constant resistivity and seismic velocity. We show that the combined SCG/ATC approach reduces the presence of artifacts both with respect to individual inversion of the resistivity and seismic datasets as well as with respect to the joint inversion of both data sets at each time step. We also performed a synthetic study using a secondary oil recovery problem. The combined CP/ATC approach is successful in retrieving the position of the oil/water encroachment front.

Introduction

The time-lapse joint inversion of geophysical data is required to solve a number of problems such as the management of oil and gas reservoirs, the sequestration of carbon dioxide, the leakage of water in earth dams and embankments through internal erosion, bioremediation, the production of geothermal reservoirs, and the monitoring of active faults and volcanoes (Lazaratos and Marion, 1997; McKenna et al., 2001; Kowalsky et al., 2006; Ajo-Franklin et al., 2007a, b; Miller et al., 2008; Doetch et al., 2010; Ayeni and Biondi, 2010; Liang et al., 2011).

Two types of strategies can be used in the joint inversion problem of geophysical data. Historically, the first strategy has been based on petrophysical models (Cross Petrophysical CP-based approach) connecting geophysical methods (e.g., Hertrich and Yaramanci, 2002; Rabaute et al., 2003; Kowalsky et al., 2006; Woodruff et al., 2010). The second approach, developed more recently, is based on the use of structural similarities between the physical properties and is called the Structural Cross-Gradient (SCG) approach (see Gallardo and Meju, 2003, Linde et al., 2006, 2008).

Several strategies are also possible for the time-lapse inversion of geophysical datasets (Vesnaver et al., 2003). The approach of separately inverting different time snapshots and comparing the results does not work in most cases because of the contamination of the inverted models by the data noise. Sequential time-lapse inversion is generally successful (e.g., Day-Lewis et al., 2002; Martínez-Pagán et al., 2010; Karaoulis et al., 2011a); however, the result is highly sensitive to the inversion of the first snapshot of the specific physical process under study. Errors made in the first tomogram can propagate through the sequence of inverted tomograms and the resulting artifacts can be substantial. The Active Time-Constrained (ATC) approach of Kim and Karaoulis (Kim et al., 2009; Karaoulis et al., 2011a, b) offers an alternative and reliable approach to simultaneously invert a complete time-lapse geophysical dataset using a time-based regularization term into a generalized cost function to minimize these artifacts.

Until recently, very few time-lapse joint inversions of geophysical data have been published. A time-lapse joint inversion algorithm of electrical direct current (DC) resistivity and georadar data has been developed by Doetch et al. (2010). Their time lapse inversion is based on the difference in the inverted results (see LaBrecque and Yang, 2001). That is, this approach minimizes the inverted results differences with respect to a background model separately at each time step. In our approach, time is introduced to the system and encompasses all the models investigated during the entire monitoring period. Therefore, in our case, the cost function of the problem contains a data misfit term corresponding to the entire dataset (i.e., the set of snapshots over the monitored period of time and the different geophysical methods).

In the present work, we combine the SCG or CP inversion approaches and the ATC time-lapse inversion to invert cross-hole synthetic data. We then discuss the advantages in combining these two approaches together, with a focus for the monitoring of partial saturation changes for the secondary recovery problem within oil reservoirs.

Description of the Geophysical Methods

Governing Equations for the DC conductivity problem

In this section, we describe the modeling of the electrical voltage potential, given the resistivity subsurface structure. The 3-D potential field due to a known DC current injection is related to the conductivity structure via a 3D Poisson equation for the electrical potential

$$-\nabla \cdot [\sigma(x,y,z)\nabla V(x,y,z)] = I\delta(x-x_s)\delta(y-y_s)\delta(z-z_s), \tag{1}$$

where the point $S(x_s, y_s, z_s)$ denotes a source current injection point where a current of magnitude I (in A) is injected (I>0) or retrieved (I <0). In equation 1, the electrical potential V (in V) is the electrical potential field in the space domain ($\mathbf{E} = -\nabla V$ represents the quasi-static electrical field in V m^{-1}), $\sigma(x, y, z) = 1/\rho(x, y, z)$ denotes the electrical conductivity (in S m^{-1}), ρ denotes the resistivity in ohm m, and δ represents the delta function.

Dey and Morisson (1979) showed that equation 1 can be efficiently solved in the 2.5D domain using a Fourier transform. The forward and inverse Fourier-cosine transforms for the electrical potential are defined as:

$$\tilde{V}(x, k_y, z) = \int_0^\infty V(x, y, z)\cos(k_y y)dy, \tag{2}$$

$$V(x, y, z) = \frac{2}{\pi}\int_0^\infty \tilde{V}(x, k_y, z)\cos(k_y y)dk_y, \tag{3}$$

respectively, and where k_y denotes the wave-number. Applying the forward transform to equation 1, we obtain the solution for the 2.5D transformed electric potential

$$-\nabla \cdot \left[\sigma(x, z)\nabla\tilde{V}(x, k_y, z)\right] + k_y^2\sigma(x, z)\tilde{V}(x, k_y, z) = \frac{I}{2}\delta(x - x_s)\delta(z - z_s). \tag{4}$$

We use a 2.5D model below. Equation 4 can be solved with the finite element method (FEM). The mesh will be based on unstructured triangular elements, where resistivity is assumed constant in each element, and the electrical potential values vary linearly within each element. The solution from the FEM provides the electrical potential at each node of the triangles, which can be transformed into an apparent resistivity.

We discuss now the calculation of the Jacobian matrix $\mathbf{J}$. Like within any inversion algorithm making use of gradient information, the partial derivatives with respect to the model parameters, the so-called sensitivities, must be known. These derivatives are of the following form $J_{ij} = \partial V_i / \partial \sigma_j$, where V_i denotes the electrical potential on the node i of the domain, and σ_j

denotes the conductivity of the j-th cell. A very efficient and therefore common approach to compute sensitivities in resistivity and electromagnetic inversion problems at the receivers is based on the principle of reciprocity (see for details Tripp et al., 1984). This requires that each electrode acts as a source and a receiver, but since the forward problem has to be solved for each electrode anyway, sensitivities can be obtained with little extra effort. An elegant way of deriving an appropriate sensitivity expression via reciprocity starts directly from the linear FEM equations (see Rodi, 1976; Oristaglio and Worthington, 1980 for further details).

The sensitivity $\frac{\partial V_{i,l}}{\partial \sigma_j}$, corresponding to a potential $V_{i,l}$ at a node i due to a source at node l, can be represented as a superposition of potentials $V_{i,m}$ originated from “fictitious” sources at the nodes m of the j-th domain element (Sasaki, 1989). Using the "principle or reciprocity", the values $V_{i,m}$ can be expressed via electrical potentials $V_{m,i}$ at the nodes m due to a current I_i at node i. The yields:

$$\frac{\partial V_{i,l}}{\partial \sigma_j} = -\frac{1}{I_i}\sum_m \sum_n a_{j_{mn}} V_{m,i} V_{n,l}, \tag{5}$$

where the double sum is made over all nodes m and n of the respective elements, and $a_{j_{mn}}$ denotes the $(m,\ n)$-th of the finite element matrix $(K_{1_j} + k_y^2 K_{2_j})$ where K_1 and K_2 denote the finite element matrices, which depend only on the nodal coordinates and element shape. The explicit form of those matrices can be found for instance in Tsourlos (1995).

Governing equations for the seismic problem

We describe now the forward problem to model the propagation of the seismic wave in an elastic material. The subsurface is discretized on a grid of nodes. A value of the slowness (inverse of the velocity) is assigned to each node. To calculate the travel times of seismic waves from seismic source to receivers, we solve the Eikonal equation,

$$\left|\nabla T(x,y,z)\right| = s(x,y,z)\,, \tag{6}$$

with the fast marching method (e.g., Sethian and Popovici, 1999; Rawlinson and Sambridge, 2005; Hassouna and Farag, 2007). In equation 6, T denotes the travel time field and s is the slowness (inverse of the velocity). In equation 6, the term $\left|\nabla T(x,y,z)\right|$ can be approximated by a second-order finite-difference scheme to increase the accuracy of the forward modeling algorithm. The explicit form of this scheme is presented by Hassouna and Farag (2007) and Kroon (2011). This yields,

$$\max(D_{ij}^{-x}T, D_{ij}^{+x}T, 0)^2 + \max(D_{ij}^{-z}T, D_{ij}^{+z}T, 0)^2 = S_{ij}^2 \tag{7}$$

where $D_{ij}^{-x,z}$ and $D_{ij}^{+x,z}$ are the standard backward and forward finite difference operators, respectively, at location (i, j) on the grid. The second-order backward and forward finite difference approximations of a grid between the two wells is given by,

$$D_{ij}^{-x} = \frac{3T_{i,j} - 4T_{i-1,j} + T_{i-2,j}}{2\Delta x}, \tag{8}$$

$$D_{ij}^{+x} = -\frac{3T_{i,j} - 4T_{i\mp 1,j} + T_{i\mp 2,j}}{2\Delta x}, \tag{9}$$

along the x-axis, respectively. Similar equations can be written along the z-axis. By substituting Equations 8 and 9 into equation 7, we get

$$\sum_{u=1}^{2} \max\left(\frac{3}{2\Delta_u}(T - T_u), 0\right)^2 = S_{ij}^2 \tag{10}$$

$$T_1 = \min\left(\frac{4T_{i-1,j} - T_{i-2,j}}{3}, \frac{4T_{i+1,j} - T_{i+2,j}}{3}\right), \tag{11}$$

$$T_2 = \min\left(\frac{4T_{i,j-1} - T_{i,j-2}}{3}, \frac{4T_{i,j+1} - T_{i,j+2}}{3}\right). \tag{12}$$

Sensitivities for the seismic velocities are described by the Fresnel raypath approach based on the numerical approach developed by Watanabe *et al.* (1999). Between the source point

$S(x_S, y_S)$ and receiver R located in a medium, we add the traveltimes from point S to all nodes P on the grid (t_{SP}) and the traveltimes from point R to all nodes P on the grid (t_{RP}). For each node on the grid, subtracting the traveltime from source S to receiver P $t_{SR,}$ yields the residuals δt. The Fresnel zone raypath is defined as the iso-surface with all residuals δt less than half a period f. In other words, the Fresnel zone raypath is $\delta t = t_{SP} + t_{RP} - t_{SR} < 1/(2f)$, where f is the main frequency of the seismic source, which is taken as the peak frequency of the Fourier transform of the signals recorded at each receiver. By accounting for the time the wave propagation is affected by heterogeneities proximal to the ray path, the sparseness of the ray distribution is reduced. Watanabe *et al*. (1999) proposed a numerical definition of Fresnel volumes, characterized by a weighting function w, that depends linearly on the delay of the seismic waves expressed as,

$$w = \begin{cases} 1 - 2f\,\delta t & \text{if } 0 < \delta t < 1/2f \\ 0 & \text{if } \delta t \geq 1/2f \end{cases} . \tag{13}$$

The Jacobian matrix **J** contains the derivatives of travel times with respect to the slowness values of the grid. Therefore each element of $J_{ij} = \partial T_i / \partial S_j$ shows the difference in travel time ∂T_i when slowness in node j is changed by ∂S_j. These partial derivatives are given by the following equation

$$\frac{\partial T_i}{\partial S_j} = w_j \frac{L_{P_i}}{\alpha} , \tag{14}$$

$$\alpha \equiv \sum_{k=1}^{n} w_{P_k} , \tag{15}$$

where the w_j represent the weight of the parameters, L_{P_i} represents the total length of the ray P_i, and a denotes the total weight for all parameters when the ray P_i is calculated.

Comparison of the sensitivities for a cross-well problem

We consider two boreholes A and B separated by a distance of 50 meter (see Figure 1). In both boreholes, we consider that the electrodes for the resistivity problem have a take-out of 4 meters (Figure 1a). On borehole A, we consider a seismic source every 4 meters and in borehole B, a set of geophones every 4 meters (Figure 1d). The position of the sensors is shown in the two boreholes in Figures 1a, d, g.

We compute the sensitivity for the resistivity and seismic problems for the three models. Model 1 corresponds to a homogeneous earth (resistivity 100 Ohm m and velocity 1 km/s). Note that seismic velocities can easily be below 1 km/s in unsaturated granular media (Rubino et al., 2011). As expected, resistivity shows higher sensitivity in the areas close to the electrodes while seismic shows a higher sensitivity in the center part of the model where the density of rays is higher. Therefore, as already reported in the literature (e.g., Gallardo and Meju, 2004), the resistivity and seismic problems display complementary sensitivities.

In Models 2 and 3 (see Figures 1d to 1i), we introduce a layer with properties different from the background. If we introduce a layer with a higher resistivity than the background, the sensitivity in this part of the model is lower than for the homogeneous case because the current is flowing around this layer. If we introduce a higher velocity layer, with respect to the velocity of the background, the sensitivity in this layer of the seismic method becomes higher than in the homogenous case (since the waves corresponding to the first arrivals are traveling through this layer). This exercise demonstrates that the resistivity and seismic methods are sensitive to different properties changes and a joint inversion is always beneficial because the spatial distribution of the sensitivities of these methods is complementary to each other. In the following section "Joint Inversion Strategies", we discuss both the strucctural cross-gradient and the cross-petrophysical approaches to perform the joint inversion. The choice of these methods will be discussed further below.

Joint Inversion Strategies

Below we present two strategies to perform joint inversion of two geophysical datasets. These two approaches have been broadly discussed in the recent literature (see recently Moorkamp et al., 2011). However, we will use these approaches in a time-lapse sense, investigating a co-located change in petrophysical properties, or their gradient, such as that associated with a change of saturation. Whatever the choice of the joint inversion approach, the joint time-lapse equation presented in the next section "Time-lapse cross-gradient joint inversion" will be identical.

The Structural Cross-Gradient (SCG) Approach

Gallardo and Meju (2003, 2004) proposed a structural joint inversion approach to connect the property of two physical parameters in the joint inversion of two geophysical datasets. The assumption underlying this approach is that the physical parameters of the subsurface should share the same structural similarity at the same position. This approach can be used especially when there is no general relationship between the magnitudes of the physical properties themselves (e.g., Moorkamp et al., 2011). Gallardo and Meju (2003, 2004) stated that the structural differences between two models can be represented mathematically by the vector field of the cross-product of the gradient of the two physical parameters, which is then used to build the relationship between these two models parameters. In the present case, we observe the structural differences of collocated transient changes of the physical parameters, which are used to build the same type of relationship. The cross-gradient inversion scheme therefore looks for finding a general structural similarity between different petrophysical properties (or change in petrophysical properties) provided by different geophysical methods (e.g., the resistivity and the seismic velocity in the present case). This method has been successfully used in several studies for both 2D and 3D problems (e.g., Gallardo et al., 2005; Tryggvason and Linde, 2006; Linde et al., 2006; Fregoso and Gallardo, 2009). In the present work, we use the P-wave velocity and DC-resistivity data but the approach can be developed for any type of geophysical data including potential field data (Gallardo, 2007; Gallardo and Meju, 2011; Gallardo et al., 2011).

The SCG cost function proposed by Gallardo and Meju (2003, 2004) is written as,

$$\boldsymbol{q}(x,y,z) = \nabla m_r(x,y,z) \times \nabla m_s(x,y,z)\,, \tag{16}$$

where m_r and m_s denote the resistivity and velocity distributions, respectively (defined here in 3D), ∇m_r and ∇m_s denote the gradients of the resistivity and velocity, respectively, and "×" denotes the cross-product operator between two vectors. In the following, we consider a discrete representation of the gradient to avoid the divergence of the gradient operator for piece-wise continuous materials. The cross-gradient approach does not need discontinuities of the physical properties as such. This is an advantage of this approach, which permits the application of the technique on smoothed models of common use in geophysics. If the resistivity and seismic models share the same discontinuity, the SCG cost function $\boldsymbol{q}(x,y,z)$ is equal to zero (as $\boldsymbol{q}$ corresponds to positive and negative values, we consider only its norm to define a positive "cost" function to minimize). Based on equation 16, the inversion is therefore seeking to minimize the cross-product of the resistivity gradient and the P-wave velocity gradient. For the time-lapse inversion described below, the inversion will seek to minimize the cross-product of the gradient of the transient resistivity changes and the gradient of the transient velocity change. We will justify this approach below directly from the petrophysics.

In this work, a 2.5-D model is assumed (y denotes the strike direction perpendicular to the two wells). In this case, Gallardo and Meju (2004) showed that the norm of $\boldsymbol{q}$ can be expressed as,

$$q(x,z) \cong \frac{4}{\Delta x \Delta z}(m_{rc}(m_{rc} - m_{rc}) + m_{rr}(m_{sc} - m_{sb}) + m_{rb}(m_{sr} - m_{sc})), \tag{17}$$

where the first subscript r or s denotes the cell of the resistivity or velocity model respectively and the second subscript c, b or r shows the center, bottom or right of each cell of the respective model (see Figure 2), and Δx and Δz denote the horizontal and vertical dimensions of each cell.

The Cross-Petrophysical (CP) Approach

In our second approach used for the joint time-lapse inversion, we follow a completely different philosophy for the joint inversion problem by using the Cross-Petrophysical Approach. This second approach uses theoretical or empirical relationships between two petrophysical properties involved in the two geophysical methods (in the present case, resistivity and velocity, Lee, 2002; Finsterle and Kowalsky 2006, Kowalsky et al., 2006; Colombo et al., 2007; Jegen-Kulcsar et al., 2009).

To include the term corresponding to the cross-relationship into the inversion, we used the CP cost function.

$$\boldsymbol{q} = [\boldsymbol{I} \quad -\mathrm{diag}(\boldsymbol{r}) * \boldsymbol{I}]\begin{bmatrix}\boldsymbol{m}_r \\ \boldsymbol{m}_s\end{bmatrix}, \tag{18}$$

where $\boldsymbol{I}$ is the $L \times L$ identity matrix (L refers to the number of cells), and $\boldsymbol{r}$ is a $L \times L$ diagonal matrix that expresses the relationships between the two properties, the subscript r and s refers to resistivity and seismic, respectively, and $\mathbf{m}_r$ and $\mathbf{m}_s$ are $L \times 1$ vectors corresponding to resistivity and seismic velocity data, respectively. The cross-petrophysical relationship between the physical parameters can be determined through site-dependent empirical relationships (based on laboratory data or downhole measurements) or through theoretical petrophysical models obtained by upscaling local equations using the same texture (e.g., Revil and Linde, 2006). The CP approach will be used below in a time-lapse sense and not in an absolute sense, as is used in most of the previous works (e.g., Moorkamp et al., 2011).

Combined Approaches

The CP approach can be used to derive cross-physical properties (e.g., Linde et al., 2006) and alternatively the SCG-approach could be used to determine the degree of structural similarity in a time-lapse problem to determine for instance a saturation front. These two approaches could be used together by adding the regularization terms for both the SCG and CP approaches to the global cost function to minimize. Such a combined approach will be investigated in more details within a future work.

Time-lapse cross-gradient joint inversion

We present now the joint ATC algorithm developed by Kim and Karaoulis (Kim et al., 2009; Karaoulis et al., 2011a, b). The rationale for a cross-gradient time-lapse approach can be discussed for a change of the water saturation over time. For example, during CO_2 sequestration or water flooding, a change of water saturation yields a change of resistivity (e.g., Archie, 1942; Waxman and Smits, 1968; Revil et al., 1998; Revil et al., 2011) and a change in the P-wave velocity (e.g., White, 1975; Rubino et al., 2011). Therefore areas associated with a change in the water saturation correspond to areas associated with a collocated change in both the DC resistivity and the seismic velocity. In some sense, the use of the cross-gradient approach is therefore even more justified for time-lapse problems than for static problems. This idea is discussed further below in the section entitled "Rational for the structural joint inversion applied to time-lapse problem ".

In our joint 2.5D-ATC approach, the subsurface is defined as a space-time model, which encompasses all space models during the entire monitoring period. In the same manner, the entire monitoring data are defined using spatial coordinates plus time. Therefore the subsurface model $\tilde{\boldsymbol{X}}$ is sparsely sampled at some pre-selected times and is expressed as $\tilde{\boldsymbol{X}} = [\boldsymbol{X}_1, \cdots, \boldsymbol{X}_t]^T$, where $\boldsymbol{X}_i = [\boldsymbol{X}_{ri}\ \boldsymbol{X}_{si}]$ is the reference resistivity and velocity space model for the ith time step and t is the number of monitoring times. The data misfit vector is defined in the space-time domain by the following function,

$$\boldsymbol{e} = \hat{\boldsymbol{D}} - G(\tilde{\boldsymbol{X}}^{k+1}) = \hat{\boldsymbol{D}} - G(\tilde{\boldsymbol{X}}^{k} + d\tilde{\boldsymbol{X}}) \tag{19}$$

In equation 19, the vector $\hat{\boldsymbol{D}}$ corresponds to the data vector defined in the spatial coordinate system (3 space coordinates and time) by $\hat{\boldsymbol{D}} = [\boldsymbol{d}_1, \cdots, \boldsymbol{d}_t]^T$, where $\boldsymbol{d}_i = [\boldsymbol{d}_{ri}\ \boldsymbol{d}_{si}]$ denotes the data from the resistivity and seismic surveys at time step i. The term $G(\tilde{\boldsymbol{X}}^k)$ denotes the forward modeling response for the resistivity ($G_1(X_r)$) and velocity ($G_2(X_s)$) expressed as,

$$G(\tilde{\boldsymbol{X}}^k) = \begin{bmatrix} G_1(X_r) \\ G_2(X_s) \end{bmatrix} \tag{20}$$

and $d\tilde{\boldsymbol{X}} = [d\boldsymbol{X}_1, \cdots, d\boldsymbol{X}_t]^T$ is the model perturbation vector for both resistivity and velocity, i.e. $d\tilde{\boldsymbol{X}} = \tilde{\boldsymbol{X}}^{k+1} - \tilde{\boldsymbol{X}}^{k}$, where the superscript k denotes the iteration number.

Having defined both the data and the model using the 4 coordinates mentioned above, the modified 2.5D-ATC algorithm will adopt two regularizations in the time and space domains to stabilize the inversion, as well as an additional regularization for the joint inversion problem. The objective function G can be expressed by (Zhang et al., 2005; Kim et al., 2009),

$$G = \boldsymbol{e}^T \boldsymbol{e} + \lambda\Psi + \alpha\,\Gamma + \omega q\,, \tag{21}$$

where Ψ and Γ are the two regularization functions for space and time and q denotes the cross gradient function (equation 16 for the SCG approach) or alternatively the cross-relationship function (equation 18 for the CP approach). The model parameterization will be in log space for the resistivity (log Ohm m) and linear space for velocities (expressed in km/s), such that both petrophysical properties will be on the same order of magnitude. The function Ψ is used for smoothness regularization in space and expressed as a second order differential operator applied to the model perturbation vector. The function Γ is used as a smoothness regularization term in time and it is expressed as a first order differential operator to the space-time model. The two parameters λ and α are the Lagrangian multipliers for controlling the two regularizations terms and the parameter ω denotes the Lagrangian multiplier for controlling the cross-gradient or cross-petrophysical functions. In our approach, the space-domain Lagrangian is expressed as a diagonal matrix $\hat{\boldsymbol{A}}$ (Yi *et al*., 2003) and the time-domain Lagrangian is expressed as a diagonal matrix $\hat{\boldsymbol{A}}$ (Karaoulis et al., 2011a, b).

Using a combination of the structural inversion and ATC inversion, our inversion algorithm favors updated models that fulfill three criteria (*1*) they should be smooth in the space domain, (2) they should be smooth in the time domain, and (3) they should show structural similarities in both resistivities and velocities changes (SCG approach) or similarities in the change of the petrophysical properties (CP approach, see the variable q in equation 18). In other words, the inversion seeks to find a space-time smooth model where similar changes are observed from both resistivity and seismic data. The objective function G to minimize is given by:

$$G = \|\boldsymbol{e}^T\boldsymbol{e}\|^2 + (\partial^2 d\hat{\boldsymbol{X}})^T \hat{\boldsymbol{\Lambda}}(\partial^2 d\hat{\boldsymbol{X}}) + \left\{\boldsymbol{M}(\boldsymbol{X}^k + d\boldsymbol{X})\right\}^T \boldsymbol{AM}(\boldsymbol{X}^k + d\boldsymbol{X}). \quad (22)$$

Minimizing G with respect to the model perturbation vector yields the following normal equations (Kim et al., 2009):

$$\tilde{\boldsymbol{X}}^{k+1} = \tilde{\boldsymbol{X}}^k + d\tilde{\boldsymbol{X}}, \quad (23)$$

$$d\tilde{\boldsymbol{X}} = \left(\hat{\boldsymbol{j}}^T\hat{\boldsymbol{j}} + \hat{\boldsymbol{C}}^T\hat{\boldsymbol{\Lambda}}\hat{\boldsymbol{C}} + \boldsymbol{M}^T\boldsymbol{AM}\right)^{-1}\left[\hat{\boldsymbol{j}}^T(\boldsymbol{DT}) - \boldsymbol{M}^T\boldsymbol{AM}\tilde{\boldsymbol{X}}^k\right], \quad (24)$$

where,

$$\boldsymbol{DT} = \begin{bmatrix} \boldsymbol{DT_1} \\ \vdots \\ \boldsymbol{DT_t} \end{bmatrix}, \quad (25)$$

$$\boldsymbol{DT_i} = \begin{bmatrix} \boldsymbol{G_1}(\boldsymbol{X_{ri}^k}) - \boldsymbol{d_{ri}} \\ \boldsymbol{G_2}(\boldsymbol{X_{si}^k}) - \boldsymbol{d_{si}} \\ -\boldsymbol{\omega} * \nabla\boldsymbol{m_r^k}(x,y,z) \times \nabla\boldsymbol{m_s^k}(x,y,z) \end{bmatrix}, \quad (26)$$

for the SCG approach and

$$\boldsymbol{DT_i} = \begin{bmatrix} \boldsymbol{G_1}(\boldsymbol{X_{ri}^k}) - \boldsymbol{d_{ri}} \\ \boldsymbol{G_2}(\boldsymbol{X_{si}^k}) - \boldsymbol{d_{si}} \\ -\boldsymbol{\omega} * (\boldsymbol{X_{ri}^k} - diag(\boldsymbol{r}) * \boldsymbol{X_{si}^k}) \end{bmatrix}. \quad (27)$$

for the CP approach. $\hat{\boldsymbol{j}}$ denotes the joint sensitivity matrix. This matrix is expressed as a block diagonal matrix $\hat{\boldsymbol{j}}$= diag $(\boldsymbol{J}_1,...,\boldsymbol{J}_t)$ where,

$$\boldsymbol{J_i} = \begin{bmatrix} \boldsymbol{J_{ri}^k} & \boldsymbol{0} \\ \boldsymbol{0} & \boldsymbol{J_{si}^k} \\ \boldsymbol{\omega} * \boldsymbol{J_{qi}^k} & \end{bmatrix} \quad (28)$$

This equation involves the cross-gradient term and $\boldsymbol{J}_{ri}^{k}$ and $\boldsymbol{J}_{si}^{k}$ denote ($n_1 \times L$) and ($n_2 \times L$) matrices corresponding to the Jacobians for the resistivity and velocity models, respectively at iteration k at time step i. The $L \times 2L$ matrix $\boldsymbol{J}_{qi}^{k}$ involves the partial derivatives of the vector $\boldsymbol{q}$ defined by equation 16. The parameter L denotes the number of cells. The parameters n_1 and n_2 denote the number of measurements for the resistivity and seismic data for each time step, respectively. The explicit form of $\boldsymbol{J}_{qi}^{k}$ can be found in Gallardo and Meju (2004). The matrix $\hat{\boldsymbol{C}}$ denotes the differential operator in the space coordinates while $\boldsymbol{M}$ denotes the differential operator in the time domain.

For the CPA approach, the form of the sensitivity matrix is given by

$$\boldsymbol{J}_{\boldsymbol{i}} = \begin{bmatrix} \boldsymbol{J}_{ri}^{k} & \boldsymbol{0} \\ \boldsymbol{0} & \boldsymbol{J}_{si}^{k} \\ \boldsymbol{\omega} * \boldsymbol{I} & -\boldsymbol{\omega} * diag(\boldsymbol{r}) * \boldsymbol{I} \end{bmatrix}. \tag{29}$$

Finally, note the model parameterization is in log space for resistivities (log Ohm m), and linear for velocities (expressed in km s^{-1}), so both of them are in the same order of magnitude.

Rational for the structural joint inversion applied to time-lapse problems

General Formulation

We have hypothesized that the model changes are structurally coupled for the electrical conductivity and the P-wave seismic velocity. Now, we explain some mechanisms for this to happen within a real field scenario. We consider clayey sand or a clayey sandstone that is water-wet. The conductivity σ of the porous material as a function of the water saturation can be written as (e.g., Jougnot et al., 2010)

$$\sigma = \frac{1}{F} s_w{}^n \left(\sigma_w + \beta_S \frac{\bar{Q}_V}{s_w{}^n} \right), \tag{30}$$

where n is the saturation exponent (Archie, 1942), s_w denotes the water saturation (s_w =1 for water-saturated porous materials), F (dimensionless) denotes the formation factor, which is related to the connected porosity ϕ (dimensionless) by Archie's law $F = \phi^{-m}$ (Archie, 1942), m (>1, dimensionless) is called the cementation exponent, σ_w denotes the conductivity of the pore water (in S m^{-1}), β_S denotes the mobility of the cations of the electrical diffuse layer and responsible for surface conductivity, and $\bar{Q}_V$ denotes the excess of charge of the electrical diffuse layer per unit pore volume. The temperature dependence of the electrical conductivity can be approximated by $\sigma(T) = \sigma(T_0)\left(1+\alpha_\sigma(T-T_0)\right)$, where $\alpha_\sigma \approx 0.023$°C^{-1}. The conductivity of the pore is proportional to the total dissolved solids (TDS) of the pore water (the conversion factor depends on the chemical composition of the pore water and can be in the range 0.54 – 0.96; a typical conversion at 25°C is (TDS) in ppm = Conductivity in µS/cm × 0.67.

For time-lapse problems characterized by a change of saturation s_w, a change in porosity ϕ, a change in temperature T, and a change in pore water conductivity (corrected for temperature), the change in the gradient of the conductivity between two times characterized by a change in the water saturation is given by,

$$\nabla\sigma = \left(\frac{\partial\sigma}{\partial s_w}\right)\nabla s_w + \left(\frac{\partial\sigma}{\partial\phi}\right)\nabla\phi + \left(\frac{\partial\sigma}{\partial T}\right)\nabla T + \left(\frac{\partial\sigma}{\partial \mathrm{TDS}}\right)\nabla(\mathrm{TDS}), \tag{31}$$

and where the derivatives of the conductivity with respect to the different key-variables are given by,

$$\left(\frac{\partial\sigma}{\partial s_w}\right) = \frac{n}{F} s_w^{\,n-1}\sigma_w. \tag{32}$$

$$\left(\frac{\partial\sigma}{\partial\phi}\right) \approx m\phi^{m-1} s_w^{\,n}\sigma_w. \tag{33}$$

$$\left(\frac{\partial \sigma}{\partial T}\right) = \sigma(T_0)\alpha_\sigma . \quad (34)$$

$$\left(\frac{\partial \sigma}{\partial \mathrm{TDS}}\right) = \frac{0.67}{F} s_w{}^n . \quad (35)$$

We turn now our attention to the seismic P-wave problem. Assuming that the viscous coupling between the pore water and the solid phase can be neglected, the velocity of the P-waves, are approximated by the Biot-Gassmann equations (Gassmann, 1951),

$$V_p{}^2 = \frac{K_u + \frac{4G}{3}}{\rho} , \quad (36)$$

where the bulk density ρ (in kg m^{-3}) and the undrained bulk modulus K_u (in Pa) are defined by,

$$\rho = (1-\phi)\rho_s + \phi\rho_f , \quad (37)$$

$$K_u = \frac{K_f(K_s - K_{fr}) + \phi K_{fr}(K_s - K_f)}{K_f(1-\phi - K_{fr}/K_s) + \phi K_s} , \quad (38)$$

where K_{fr} and G denote the drained modulus and the shear modulus of the skeleton (both independent on the water saturation and in Pa), and K_s denotes the bulk modulus of the solid phase. In unsaturated conditions, we consider that the density of the pore fluid ρ_f and the bulk modulus of the pore fluid K_f are related to the properties of the gas (subscript g) and water (subscript w) by the following relationships (Teja and Rice, 1981)

$$\rho_f = (1-s_w)\rho_g + s_w\rho_w , \quad (39)$$

$$\frac{1}{K_f} = \frac{1-s_w}{K_g} + \frac{s_w}{K_w} . \quad (40)$$

The change in the gradient of the velocity can be therefore written as,

$$\nabla V_p = \left(\frac{\partial V_p}{\partial s_w}\right)\nabla s_w + \left(\frac{\partial V_p}{\partial \phi}\right)\nabla \phi + \left(\frac{\partial V_p}{\partial T}\right)\nabla T + \left(\frac{\partial V_p}{\partial \mathrm{TDS}}\right)\nabla \mathrm{TDS} . \quad (41)$$

The seismic velocity dependence on the salinity (last term of equation 41) is pretty small (see Wyllie et al., 1956, their Figure 3). This effect corresponds to osmotic effects responsible for chemio-osmotic poroelastic changes (e.g., Revil 2007). It can be generally neglected except in shales.

Monitoring the Secondary Recovery of Oil

If the porosity change is of poroelastic nature and therefore relatively small, the gradient change in the conductivity can be approximated by,

$$\nabla\sigma \approx \left(\frac{\partial\sigma}{\partial s_w}\right)\nabla s_w, \tag{42}$$

In other words, changes in saturation and temperature are potentially more important than changes in porosity in terms of controlling the change in the gradient of the electrical conductivity.

The term associated with changes in temperature is vanishingly small in thermoporoelasticity (it can be computed from the formulation given by McTigue, 1986 for instance) except in the case of heavy hydrocarbons (Martinez et al., this issue). In poroelasticity, the term related to variations in porosity (generally through a change in the effective stress) is expected to be also pretty small by comparison with the first term. For clayey sandstone, Han et al. (1986) found the following correlation between the P-wave velocity, the porosity, and the volumetric clay content C ($0 \leq C \leq 0.5$): V_P (km/s) = 5.59 - 6.93 ϕ - 2.18 C. This means that a change of 1% in porosity can be responsible for a change of approximately 70 m s^{-1} for the P-wave velocity. Conversely, a modification of saturation is responsible for a strong variation on the P-wave velocity (see Figure 3a). Therefore,

$$\nabla V_p \approx \left(\frac{\partial V_p}{\partial s_w}\right)\nabla s_w, \tag{43}$$

which explains why 4D seismic imaging is efficient in monitoring the production of oil and gas reservoirs. Also, it is known that the saturation dependence of the P-wave velocity tends to be larger for soft (low velocity) rocks like clayey sandstones. For the secondary recovery of oil by water flooding, the effect of saturation dominates the response for the P-wave velocity and the resistivity (see the amplitude of the changes in Figure 3 for the Berea sandstone). In this situation, the cross-product $\nabla\sigma\times\nabla V_p$ will be equal to zero. Both the SCG and CP approaches are expected to work.

Steam-Assisted Production of Heavy Oil

The in-situ production of heavy oil in sands consists of many different techniques, of which Steam Assisted Gravity Drainage (SAGD) and the Cyclic Steam Stimulation (CSS) are common. These techniques involved an increase of the temperature, an increase of the TDS of the pore water (by dissolution of some minerals), and a variation of saturation of oil. Martinez et al. (this issue) are showing the effect of temperature on both the electrical conductivity and the seismic velocities. The cross-product of the gradient of the change of the conductivity by the gradient of the change of the seismic velocity is given by:

$$\nabla\sigma\times\nabla V_p=\left(\frac{\partial\sigma}{\partial T}\right)\left(\frac{\partial V_p}{\partial s_w}\right)\left(\nabla T\times\nabla s_w\right)+\left(\frac{\partial\sigma}{\partial \mathrm{TDS}}\right)\left(\frac{\partial V_p}{\partial s_w}\right)\left(\nabla\mathrm{TDS}\times\nabla s_w\right). \qquad (44)$$

The temperature and TDS gradients are expected to be, at first approximation, colinear with the change of saturation (from the produced area to the undisturbed reservoir) and therefore, here again, the cross-product of the gradient of the conductivity change by the gradient of the velocity change is expected to be minimum. The SCG and CP approaches proposed above are expected to work because a relationship between the velocity and resistivity co-located changes associated with a change in the saturation.

CO_2 Sequestration and Gas Hydrates

In the case of CO_2 sequestration, Myer (2001) has measured substantial change in both resistivity and P-wave velocity in the laboratory in the presence of CO_2 (increase over 100 and 10%, respectively) for the Berea sandstone. The presence of CO_2 is therefore expected to create co-located gradients in both the electrical conductivity and the P-wave velocity and co-located variations in the electrical conductivity and the P-wave velocity. Therefore both the SCG and CP approaches are expected to work as well. The same would apply for the production of gas hydrates as the presence of gas hydrates has both a strong signature on both the seismic velocity and the electrical resistivity (Guerin et al., 2006).

Time-Lapse Joint Inversion: Numerical Experiments

Synthetic Problem Test

We test now our joint time-lapse inversion algorithm on a simple time-lapse problem. Figure 4a shows a set of 3 snapshots for a moving and deforming target between two wells. We show in Figure 4b the changes between snapshots 2 and 1 and between the snapshots 3 and 1. The properties of the heterogeneity and background are similar to the test discussed above. Like in the previous synthetic case, we use a bipole-bipole array for the DC resistivity (P1 and C1 electrodes in borehole A, P2 and C2 electrode in borehole B) with a total of 1100 measurements. The synthetic data are contaminated with a 3% noise level.

Figures 5, 6, and 7 show the results for independent inversion, time-lapse inversion, and cross-gradient time-lapse joint inversion, respectively. The blue colors indicate an increase in the resistivity or seismic velocity while the red colors indicate a decrease. The three types of inversion reach a data Root Mean Square (RMS) error around 3% at the 5th iteration, which corresponds to the noise level added to the data (Figure 8 shows that the data misfit function converges very quickly in two iterations). In each case, the domain where there is a true variation of the resistivity and seismic velocity is shown by the plain line. We see on this example that the cross-gradient time-lapse joint inversion improve the results of the inversion in the sense that there are much less spatial artifacts in the tomograms shown in Figure 7 as compared with the tomograms shown in Figures 5 and 6. For the joint inversion, the test results seems to show only a modest improvement: the seismic tomograms seems to get rid of the background noise. Indeed the seismic and resistivity background noises are spatially dissimilar and therefore filtered out by the joint inversion.

Figure 9 shows the model RMS error, that is, the difference between the synthetic and inversion models, by using independent inversion and the joint time-lapse inversion. Besides the smaller inversion artifacts, there is a clear improvement in the model RMS error for both resistivities and velocities models with the time-lapse joint inversion as compared with the independent inversions. Note that with the time-lapse joint inversion, the recovered modification in resistivity is on the order of 25 Ohm m while the true variation is on the order of 90 Ohm m. We cannot however increase further the number of iterations without fitting the noise. This explains the large model RMS error in the resistivity inversion as compared to the model RMS error for the velocity inversion as the relative change of velocity is smaller. Figure 10 shows the residuals after the 5th iteration, for both apparent resistivities and travel times. These residuals are very small with respect to the absolute values of the apparent resistivities and travel times.

Value of the Lagrange Parameters

We first discuss the effect of the temporal variations into the inversion scheme. The temporal changes are controlled by the matrix $\boldsymbol{A}$. Large values of the temporal Lagrange parameter result in unnecessary smoothness over time suppressing real modifications in the sequence of tomograms. At the opposite, small values of the temporal Lagrange parameter may produce inversion artifacts. Ideally, entries of the matrix $\boldsymbol{A}$ associated with areas characterized by significant changes in the petrophysical properties must be assigned low time regularization values. At the opposite, entries of the matrix $\boldsymbol{A}$ associated with areas characterized by small variations in the petrophysical properties must be assigned high time regularization values. Figure 11 displays the time related Lagrange distribution of the sequence of models. Because this model has three time-steps, only two figures are shown. They corresponds to changes from time step 1 to time step 2 and variations from time step 2 to time step 3. The areas characterized by low values of the time Lagrange parameters are in good agreement with areas characterized by a strong change in the modeled changes of the petrophysical properties (see Figure 4).

Values of the Regularization Parameters

In our algorithm, there are three regularization parameters affecting the final tomogram, which include one for the spatial regularization, one for the time-lapse regularization, and the last one for the joint inversion. Each of the regularization terms is controlled by its corresponding Lagrange parameters λ, α, and ω. By assigning different weights to each of these parameters, we can favor some characteristics of the tomogram. For instance, if we assume that we suspect no great structural connection between resistivities and velocities, the operator can perform the inversion with a small value of ω. If large temporal changes are expected, the operator can assign small values to the matrix **A**. It is not possible to suggest a global pattern for each individual case: this pattern should be adjusted based on the experience of the user.

Distribution of the Cross-Gradient function

We address now the effect of the cross-gradient function on the inversion algorithm. To illustrate our point, we consider the previous synthetic problem where the resistivity and velocity distributions are piecewise constants. Large values of the computed cross-gradient values are observed at the boundaries of the structurally constrained models as expected (see Figure 12).

Application to Water Flooding for Oil Reservoir Production

We apply now the time-lapse joint inversion algorithm to a water-flood experiment and secondary oil recovery in which water is injected in one well and the oil is produced in a second well. The governing equations, petrophysical relationships for the relative permeability and capillary pressure are described in Appendix A. The reservoir is simulated with a stochastic random generator using the petrophysical model described in Revil and Cathes (1999).

Once the saturations are computed at each time step, we compute the velocity and the resistivity from the water saturation using the properties shown in Figure 3. Figure 13 shows the porosity and permeability model. The evolution of the saturation over time is shown in Figure 14. Figure 15 illustrates the relationship between velocity and resistivity when a variation in saturation occurs. The results of Figure 14 and Figure 15 are combined together to compute the simulated resistivities and velocities for a 6 time-step models (Figure 16). The bipole-bipole resistivity and seismic sources and receivers arrays are similar to those described in the previous synthetic problem (Figure 4). Similar random noise was added to the synthetic data. In this type of model, which is characterized by a relatively sharp modification in the petrophyscal properties, we favored the CP-approach for the joint inversion instead of the SCG approach. The inverted results are shown in Figure 17a (iteration 7, data RMS error of 3%.). The evolution of the data error is shown in Figure 17b, and the algorithm converged in few iterations.

Once the resistivity and the velocity have been jointly inverted over the complete sequence of snapshots, we can see if we can recover the position of the saturation front from the inverted data. We use the second Archie's law (shown in Figures 3b) to compute the saturation from the inverted resistivity resulting from the time-lapse joint inversion. The result is shown in Figure 18a. A contour line for a function of two variables is a curve connecting points where the function has the same specified constant value. The gradient of the function is always perpendicular to the contour lines. When the lines are close to each other the magnitude of the gradient is large and the variation is steep. We develop a simple algorithm to locate the position of the oil/water interface by looking at the contour line perpendicular to the steepest gradient in the saturation. The result is shown in Figure 18b and compared to the true position of the interface. From this figure, it is clear that the kinetics and position of the oil/water interface is pretty well recovered by our time-lapse joint inversion algorithm.

Conclusions

We have proposed a new time-lapse joint inversion approach by combining the structural cross-gradient (SCG) approach or the cross-petrophysical (CP) approach with the actively-time constraint (ATC) approach. The two joint inversion approaches are justified when there is a variation of the saturation of the pore fluids in the pore space. The combination of the joint inversion and the ATC approach reduce artifacts due to noise in the data, especially when the noise is not correlated in time and space.

For a synthetic cross-well tomography test, we have evaluated the joint time-lapse inversion of DC resistivity and seismic data, which can be used to improve the monitoring of a target changing position and shape over time. This was done by generating a sequence of snapshots showing a target moving between two wells inside a homogeneous background. The SCG and CP approaches improves the localization of the areas characterized by a gradient in the resistivity and seismic velocities or simultaneous variations in the material properties, as well as takes advantage of the different and complementary sensitivities of the DC resistivity and seismic problems. We show that the joint time-lapse inversion of the resistivity and seismic data improves the image of the target for cross-well tomography.

As the time-lapse joint inversion of the geophysical data can yield a set of tomograms with a higher spatial resolution than independent inversions, this procedure is better suited to constrain both the parameter estimation process and can provide better information about the shape of a moving target such as a saturation front. In turn, the estimates of the geophysical parameters (resistivity and seismic velocities) can be used jointly to obtain a better estimate of parameters relevant to the problem (e.g., the evolution of the oil and water saturations for a secondary recovery problem). The evolution of these relevant parameters can be used in a second inversion problem to determine a second set of properties like for instance the permeability of the reservoir.

Acknowledgments. The United States Environmental Protection Agency through its Office of Research and Development partially funded and collaborated in the research described here under contract #EP10D00437 to Marios Karaoulis). It has been subjected to Agency review and approved for publication. We acknowledge funding from Chevron Energy Technology Company (Grant #CW852844) and DOE (Geothermal Technology Advancement for Rapid Development of Resources in the U.S., GEODE, Award #DE-EE0005513) for funding, Max Meju, Luis Gallardo, and two anonymous referees for their very constructive reviews and the Associate Editor, Carlos Torres-Verdín, for his work.

Appendix A. Multiphase Flow Simulation

We consider a clayey sand or sandstone with oil being the non-wetting pore fluid phase and water being the wetting pore fluid phase. In the following, s_w and s_o denote the water and oil saturation, respectively ($s_o + s_w = 1$), and s_{wr} and s_{or} denote the residual water and oil saturations, respectively. We consider the two continuity equations for the mass balance of the water and oil fluid phases (e.g., Pedlosky, 1987):

$$-\nabla \cdot (\rho_o \boldsymbol{u}_o) + (\rho_o \hat{q}_o) = \frac{\partial(\rho_o \phi S_o)}{\partial t}, \tag{A1}$$

$$-\nabla \cdot (\rho_w \boldsymbol{u}_w) + (\rho_w \hat{q}_w) = \frac{\partial(\rho_w \phi S_w)}{\partial t}, \tag{A2}$$

where ρ_o = 644 kg m^{-3} and ρ_w = 1000 kg m^{-3} denote the mass densities of oil and water, respectively, $\boldsymbol{u}_o$ and $\boldsymbol{u}_w$ denote the oil and water Darcy velocities $(\mathrm{m\,s^{-1}})$, respectively, ϕ denotes the connected porosity, $\hat{q}_o$ and $\hat{q}_w$ are oil and water source volumetric flux in $(\mathrm{m^3\ s^{-1}})$. The Darcy velocities $\boldsymbol{u}_o$ and $\boldsymbol{u}_w$ are given by the following Darcy constitutive equations (e.g., Helmig *et al.*, 1998).

$$\boldsymbol{u}_o = -\frac{k_{ro}(s_o)k}{\mu_o}(\nabla p_{cow}(s_w) - \nabla p_w - \gamma_o \nabla \mathrm{D}^{\#}), \tag{A3}$$

$$\boldsymbol{u}_w = -\frac{k_{rw}(S_w)k}{\mu_w}\left(\nabla p_w - \gamma_w \nabla \mathrm{D}^{\#}\right), \tag{A4}$$

where $\gamma_o = 6371$ Pa m^{-1} and $\gamma_w = 9900$ Pa m^{-1} denote the specific gravity for the oil and water, respectively, k denotes the intrinsic permeability of the porous material (for our isotropic case k is a scalar expressed in m^2), $k_{ro}(s_o)$ and $k_{rw}(s_w)$ are dimensionless relative permeabilities, non-linear functions of saturations, and pcow denote the capillary pressure function, and

$\nabla D^{\#} = 2.5$ m is the fixed depth change here. The oil pressure is $p_w - p_{cow}(s_w)$ where $p_{cow}(s_w)$ is water-oil capillary pressure (in Pa), a nonlinear function of water saturation s_w. We use the following expressions for the relative permeabilities and capillary pressure functions (e.g., Helmig. et al., 1998; Braun et al., 2005; Saunders et al., 2006):

$$k_{rw}(s_w) = \begin{cases} 0 & s_w \le s_{wr} \\ k^*_{rw}\left(\dfrac{s_w - s_{wr}}{1 - s_{or} - s_{wr}}\right)^{n_w} & s_{wr} < S_w \le 1 - s_{or} \\ k^*_{rw} & s_w > 1 - s_{or} \end{cases}, \tag{A5}$$

$$k_{ro}(s_o) = \begin{cases} 0, & s_o \le s_{or} \\ k^*_{ro}\left(\dfrac{s_o - s_{or}}{1 - s_{or} - s_{wr}}\right)^{n_o}, & s_{or} < s_o \le 1 - s_{wr} \\ k^*_{ro}, & s_o > 1 - s_{wr} \end{cases}, \tag{A6}$$

$$p_{cow}(s_w) = \begin{cases} 68{,}948 \text{ Pa} & s_w \le s_{wr} \\ \beta_{\mathrm{ow}} - \alpha_{\mathrm{ow}}\left[\dfrac{s_w - s_{wr}}{1 - s_{or} - s_{wr}}\right]^{-\frac{1}{3.86}} & s_{wr} < s_w \le 1 - s_{or} \\ 0 & 1 - s_{or} < s_w \end{cases}, \tag{A7}$$

where $\mathrm{k}^*_{ro} = 0.7$ $\mathrm{k}^*_{rw} = 0.08$, $n_w = 2$ $n_o = 3$, $s_{\mathrm{or}} = 0.3$, $s_{\mathrm{wr}} = 0.25$, μ_o = 5×10^{-3} Pa s and μ_w= 0.6×10^{-3} Pa s denote the dynamic viscosity of the oil and water, respectively, α_{ow} = 18,616 Pa and β_{ow} = 18,726 Pa. We maintain a constant injection of water at the injection well (Well A in Figure 13) and a constant pressure at the production well (Well B in Figure 13). So the oil and water volumetric flux $\hat{q}_o$ and $\hat{q}_w$ are given by (see Peaceman et al., 1982)

$$\hat{q}_w = \begin{cases} -0.000082 \text{ m}^3\text{s}^{-1}, & x = 0\,\text{m}, 20\,\text{m} < z < 170\,\text{m} \\ WI\dfrac{k_{rw}(S_w)}{\mu_w}(P_w - P_{BHPP}), & x = 50\,\text{m}, 20\,\text{m} < z < 170\,\text{m} \\ 0, & \text{elsewhere} \end{cases}, \tag{A8}$$

$$\hat{q}_o = \begin{cases} WI \dfrac{k_{rw}(S_w)}{\mu_w}(P_w - P_{BHPP}), & x = 50\,\mathrm{m}, 20\,\mathrm{m} < z < 170\,\mathrm{m} \\ 0, & \text{elsewhere} \end{cases}, \tag{A9}$$

respectively, where the production pressure is controlled at p_{BHPP} = 0 Pa and WI defines the well index (Peaceman *et al*.,1982),

$$WI = \frac{(2\pi\, k\Delta z)}{\log\left(\dfrac{\sqrt{\Delta x}\sqrt{\Delta y}}{0.25\sqrt{\pi}}\right) - \dfrac{1}{2} + 2}. \tag{A10}$$

We generated the reservoir porosity and permeability using the petrophysical model of Revil and Cathles (1999) for clay sand mixtures. We define the clay volume fraction φ_v (dimensionless) and the porosity of a clay sand mixture is given by: $\phi = \phi_{sd} - \varphi_v(1-\phi_{sh})$ where $\phi_{sd} = 0.4$ denote the porosity of the clean sand end-member and $\phi_{sh} = 0.6$ denote the porosity of the shale end-member. The permeability is described by $k^{\#} = k_{sd}\left(\phi / \phi_{sd}\right)^6$ where k_{sd} denote the permeability of the clean-sand end member (2000 mD, 1 mD = 10^{-15} m^2). The spatial distribution of the volumetric clay content of the sand clay mixture, φ_v, is generated with the SGeMS library (see Stanford University, Stanford Geostatistical Earth Modeling Software, http://sgems.sourceforge.net/). We used the following semi-variogram:

$$\gamma(x,z) = 1 - \exp\left[-3\left(\frac{x^2}{17^2} + \frac{z^2}{10^2}\right)\right], \tag{A11}$$

where the distances are expressed in meters. The present approach could apply as well to carbonate rocks but a facies approach would be required to determine the porosity and permeability.

References

Ajo-Franklin, J., C. Doughty, and T. Daley, 2007a, Integration of continuous active-source seismic monitoring and flow modeling for CO_2 sequestration: The Frio II brine pilot: Eos Transactions, American Geophysical Union Fall Meeting Supplement, **88**.

Ajo-Franklin, J., B. Minsley, and T. Daley, 2007b, Applying compactness constraints to differential traveltime tomography: Geophysics, **72**, no. 4, R67–R75.

Archie, G.E., 1942, The electrical resistivity log as an aid in determining some reservoir characteristics: *Trans. Am. Inst. Min. Metall. Eng.,* **146,** 54–62.

Ayeni, G., and B. Biondi, 2010, Target-oriented joint least-squares migration/inversion of time-lapse seismic data sets: Geophysics, **75**, no. 3, R61–R73.

Braun, C., R. Helmig, and S. Manthey, 2005, Macro-scale effective constitutive relationships for two-phase flow processes in heterogeneous porous media with emphasis on the relative permeability-saturation relationship: Journal of Contaminant Hydrology, **76**, 47-85.

Colombo D., M. De Stefano, 2007, Geophysical modeling via simultaneous Joint inversion of seismic, gravity and electromagnetic data: Application to prestack depth imaging: The Leading Edge, **3**, p. 326 - 331.

Day-Lewis, F., J.M. Harris, and S. M. Gorelick, 2002, Time-lapse inversion of cross-well radar data: Geophysics, **67**, no. 6, 1740-1752.

Dey A, and H.F., Morrison, 1979, Resistivity modeling for arbitrary shaped two-dimensional structures: Geophysical Prospecting, **27**,106-136.

Doetsch J., N. Linde N., and A. Binley (2010), Structrural joint inversion of time-lapse crosshole ERT and GPR traveltime data: Geophys. Res. Letters, **37**, L24404, doi:10.1029/2010GL045482.

Fregoso, E. and L.A. Gallardo (2009), Cross-gradients joint 3D inversion with applications to gravity and magnetic data, Geophysics, **74**, no. 4, L31-L42, doi:10.1190/1.3119263.

Finsterle, S., and M. B. Kowalsky 2006, Joint hydrological-geophysical inversion for soil structure identification, PROCEEDINGS, TOUGH Symposium, Lawrence Berkeley National Laboratory, Berkeley, California, May 15-17, 2006.

Gallardo, L. A., M. A. Meju, 2003, Characterization of heterogeneous near-surface materials by joint 2D inversion of dc resistivity and seismic data: Geophys. Res. Lett., **30**, no. 13, 1658, doi:10.1029/2003GL017370.

Gallardo, L. and A., Meju, M. A., 2004, Joint two-dimensional DC resistivity and seismic time inversion with cross-gradients constrains: Journal of Geophysical Research, **109**, B03311, doi:10.1029/2003JB002716.

Gallardo, L. A., M. A. Meju, and M. A. Perez-Flores, 2005, A quadratic programming approach for joint image reconstruction: mathematical and geophysical examples: Inverse Problem, **21**, 435-452.

Gallardo, L.A. and M.A. Meju, 2011, Structure-coupled multi-physics imaging in geophysical sciences: Reviews of Geophysics, **49**, RG1003, doi:10.1029/2010RG000330.

Gallardo,L.A., S.L. Fontes, M.A. Meju, P. de Lugao and M. Buonora, 2011, Robust geophysical integration through structure-coupled joint inversion and multispectral fusion of seismic reflection, magnetotelluric, magnetic and gravity images: Example from Santos Basin, Brazil. Geophysics, submitted.

Gallardo, L. A. (2007), Multiple cross-gradient joint inversion for geospectral imaging: Geophys. Res. Lett., **34**, L19301, doi:10.1029/2007GL030409.

Gassmann, F., 1951, Über die elastizität poröser medien, *Vierteljahrsschr. Naturforsch. Ges. Zuerich*, **96**, 1–23.

Guerin, G., Goldberg, D.S., and Collett, T.S., 2006. Sonic velocities in an active gas hydrate system: Hydrate Ridge. In Tréhu, A.M., Bohrmann, G., Torres, M.E., and Colwell, F.S. (Eds.), Proc. ODP, Sci. Results, **204**, 1–38.

Han, D.H., A. Nur, and D. Morgan, 1986, Effects of porosity and clay content on wave velocities in sandstones: Geophysics, **51**, no. 11, 2093-2107.

Hassouna M. S and A.A. Farag, 2007, Multistencils fast marching methods: A highly accurate solution to the Eikonal equation on cartesian domains: IEEE Transactions on Pattern Analysis and Machine Intelligence, **29**, no. 9, 1563-1574.

Helmig R., and R. Huber, 1998, Comparison of Galerkin-type discretization techniques for two-phase flow in heterogeneous porous media: Advances in Water Resources, **21**, no. 8, 697-711.

Hertrich, M. and U. Yaramanci, 2002, Joint inversion of surface nuclear magnetic resonance and vertical electrical sounding, Journal of Applied Geophysics: **50**, no. 1-2, 179-191.

Jougnot D., A. Ghorbani, A. Revil, P. Leroy, and P. Cosenza, 2010, Spectral Induced Polarization of partially saturated clay-rocks: A mechanistic approach: Geophysical Journal International, **180**, no. 1, 210-224, doi: 10.1111/j.1365-246X.2009.04426.x.

Jun-Zhi W. and O. B. Lile, 1990, Hysteresis of the resistivity index in Berea sandstone, Proceedings of the First European Core Analysis Symposium, London, England, 427-443.

Karaoulis, M.,. J.-H. Kim, and P.I. Tsourlos, 2011a, 4D Active Time Constrained Inversion: Journal of Applied Geophysics, **73**, no. 1, 25-34.

Karaoulis M., A. Revil, D.D. Werkema, B. Minsley, W.F. Woodruff, and A. Kemna, 2011b, Time-lapse 3D inversion of complex conductivity data using an active time constrained (ATC) approach: Geophysical Journal International, **187**, 237–251, doi: 10.1111/j.1365-246X.2011.05156.x.

Kim J.-H., M.J. Yi, S.G. Park, and J.G. Kim, 2009, 4-D inversion of DC resistivity monitoring data acquired over a dynamically changing earth model: Journal of Applied Geophysics, **68**, no. 4, 522-532.

Kowalsky M. B., J. Chen, and S.S. Hubbard, 2006, Joint inversion of geophysical and hydrological data for improved subsurface characterization: The Leading Edge, **25**, no. 6, 730-734.

Kroon D.J., 2011, Accurate Fast Marching Toolbox: Matlab file exchange, http://www.mathworks.com/matlabcentral/fileexchange/24531-accurate-fast-marching.

Jegen-Kulcsar, M., R.W. Hobbs, P. Tarits, and A. Chave, 2009, Joint inversion of marine magnetotelluric and gravity data incorporating seismic constraints: preliminary results of sub-basalt imaging off the Faroe Shelf: Earth and Planetary Science Letters, **282**, 47-55.

LaBrecque, D. J., and X. Yang (2001), Difference inversion of ERT data: A fast inversion method for 3-D in situ monitoring, J. Environ. Eng. Geophys., 6(2), 83–89, doi:10.4133/JEEG6.2.83.

Lazaratos, S., and B. Marion, 1997, Crosswell seismic imaging of reservoir changes caused by CO_2 injection: The Leading Edge, **16**, 1300–1306.

Lee W. M., 2002, Joint inversion of acoustic and resistivity data for the estimation of gas hydrate concentration, U.S. Geological Survey Bulletin 2190.

Liang, L., A. Abubakar, and T. M. Habashy, 2011, Estimating petrophysical parameters and average mud-filtrate invasion rates using joint inversion of induction logging and pressure transient data: Geophysics, **76**, no. 2, E21-E34.

Linde, N., A. Binley, A. Tryggvason, L. B. Pedersen, and A. Revil, 2006, Improved hydrogeophysical characterization using joint inversion of cross-hole electrical resistance and ground-penetrating radar traveltime data: Water Resour. Res., **42**, W12404, doi:10.1029/2006WR005131.

Linde, N., A. Tryggvason, J. E. Peterson, and S S. Hubbard, 2008, Joint inversion of crosshole radar and seismic traveltimes acquired at the South Oyster Bacterial Transport Site: Geophysics, **73**, no. 4, G29-G37.

Martinez F. J., M L. Batzle, and A. Revil, 2012, Influence of temperature on seismic velocities and complex conductivity of heavy oil bearing sands, in press in Geophysics.

Martínez-Pagán P., A. Jardani, A. Revil, and A. Haas, 2010, Self-potential monitoring of a salt plume: Geophysics, **75**, no. 4, WA17–WA25, doi: 10.1190/1.3475533.

McKenna, J., D. Sherlock, D., and B. Evans, 2001, Time-lapse 3-D seismic imaging of shallow subsurface contaminant flow: Journal of Contaminant Hydrology, **53**, no.1-2, 133-150.

McTigue, D.F., 1986, Thermoelastic response of fluid-saturated porous rock: J. Geophys. Research, **91**, no. B9, 9533-9542.

Miller, C. R., P. S. Routh, T. R. Brosten, and J. P. McNamara, 2008, Application of time-lapse ERT imaging to watershed characterization: Geophysics, **73**, no. 3, G7–G17.

Moorkamp, M., B. Heincke, M. Jegen, A. W. Roberts, and R. W., Hobbs, 2011, A framework for 3-D joint inversion of MT, gravity and seismic refraction data: *Geophys. J. Int*., **184**, 477–493, doi: 10.1111/j.1365-246X.2010.04856.x.

Myer, L.R., 2001, Laboratory Measurement of Geophysical Properties for Monitoring of CO_2 Sequestration, Proceedings of First National conference on Carbon Sequestration, 9 pp.

Oristaglio, M.L., and M.H. Worthington, 1980, Inversion of surface and borehole electromagnetic data for two-dimensional electrical conductivity models, Geophysical Prospecting, **28**, no. 4, 633-657.

Peaceman, D.W., 1982, Interpretation of Well-Block Pressures in Numerical Reservoir Simulation With Nonsquare Grid Blocks and Anisotropic Permeability, paper SPE 10528, presented at the 1982 SPE Symposium on Reservoir Simulation, New Orleans, Jan 31-Feb 3 1982.

Pedlosky, J., 1987, Geophysical fluid dynamics: Springer, ISBN 9780387963877.

Rabaute, A., A. Revil, and E. Brosse, 2003, In situ mineralogy and permeability logs from downhole measurements. Application to a case study in clay-coated sandstone formations: Journal of Geophysical Research, **108**, 2414, doi: 10.1029/2002JB002178.

Rawlinson N. and M. Sambridge, 2005, The fast marching method: an effective tool for tomographic imaging and tracking multiple phases in complex layered media: Exploration Geopysics, **36**, 341-350.

Revil, A., L.M. Cathles, S. Losh,. and J.A. Nunn, 1998, Electrical conductivity in shaly sands with geophysical applications: *J. Geophys. Res.,* **103**, no. B10, 23 925–23 936.

Revil, A., and L.M., Cathles, 1999, Permeability of shaly sands: Water Resources Research, **35**, no. 3, 651-662.

Revil, A., and N. Linde, 2006, Chemico-electromechanical coupling in microporous media, Journal of Colloid and Interface Science, **302**, 682-694.

Revil, A., 2007, Thermodynamics of transport of ions and water in charged and deformable porous media: Journal of Colloid and Interface Science, **307**, no. 1, 254-264.

Revil A., M. Schmutz, and M.L. Batzle, 2011, Influence of oil wettability upon spectral induced polarization of oil-bearing sands: Geophysics, **76**, no. 5, A31-A36.

Rodi, W. L., 1976, A technique for improving the accuracy of finite element solutions for magnetotelluric data: Geophys. J. R. astr. Soc., **44**, 483-506.

Rubino, J.G., D.R.Velis, and M.D. Sacchi, M.D., 2011, Numerical analysis of waveinduced fluid flow effects on seismic data: application to monitoring of CO_2 storage at the Sleipner Field: *J. Geophys. Res.,* **116,** B03306, doi:10.1029/2010JB007997.

Sasaki, Y., 1989. 2-D joint inversion of magnotelluric and dipole-dipole resistivity data. Geophysics, **54**, 254-262.

Saunders, J. H., M. D. Jackson, and C. C. Pain, 2006, A new numerical model of electrokinetic potential response during hydrocarbon recovery: Geophys. Res. Lett., **33**, L15316.

Sethian, J.A., and A. M. Popovici, 1999, 3-D traveltime computation using the fast marching method, Geophysics, **64**, no. 2, 516-523.

Stanford University, Stanford Geostatistical Earth Modeling Software (S-GEMS), http://sgems.sourceforge.net/

Teja, A.S. and P. Rice, 1981, Generalized corresponding states method for viscosities of liquid mixtures: Ind. Eng. Chem. Fundam.*,* **20**, 77–81.

Tripp, A., G. Hohmann, and C. Swift, 1984, Two-dimensional resistivity inversion: Geophysics, **49**, 1708-1717.

Tryggvason, A., and N. Linde, 2006, Local earthquake tomography with joint inversion for P- and S- wave velocities using structural constraints: Geophys. Res. Lett., **33**, L07303.

Tsourlos, P., 1995, Modeling interpretation and inversion of multielectrode resistivity survey data. Ph.D. Thesis, University of York, U.K.

Vesnaver, A.L., F., Accainoz, G., Bohmz, G., Madrussaniz, J., Pajchel, G. Rossiz, and G. Dal Moro, 2003, Time-lapse tomography: Geophysics, **68**, no. 3, 815–823.

Waxman, M.H. & Smits, L.J.M., 1968, Electrical conductivities in oil bearing shaly sands: Soc. Pet. Eng. J., **8,** 107–122.

Watanabe, T., T. Matsuoka, and Y. Ashida, 1999, Seismic traveltime tomography using Fresnel volume approach: Expanded Abstracts of 69th SEG Annual Meeting, SPRO12.5, **18**, 1402.

White, J., 1975, Computed seismic speeds and attenuation in rocks with partial gas saturation: Geophysics, **40,** 224–232.

Woodruff W. F., A. Revil, A. Jardani, D. Nummedal, and S. Cumella, 2010, Stochastic inverse modeling of self-potential data in boreholes: Geophysical Journal International, **183**, 748–764.

Wyllie, M.R.J., A.R. Gregory, and L.W. Gardner, 1956, Elastic wave velocities in heterogeneous and porous media: Geophysics, **21**, no. 1, 41-70.

Yi, M.-J., J.-H. Kim, and S.-H. Chung, 2003, Enhancing the resolving power of least-squares inversion with active constraint balancing: Geophysics, **68**, 931-941.

Zhang Y., A. Ghodrati, and D.H. Brooks, 2005, An analytical comparison of three spatio-temporal regularization methods for dynamic linear inverse problems in a common statistical framework: Inverse Problems, **21**, 357–382.

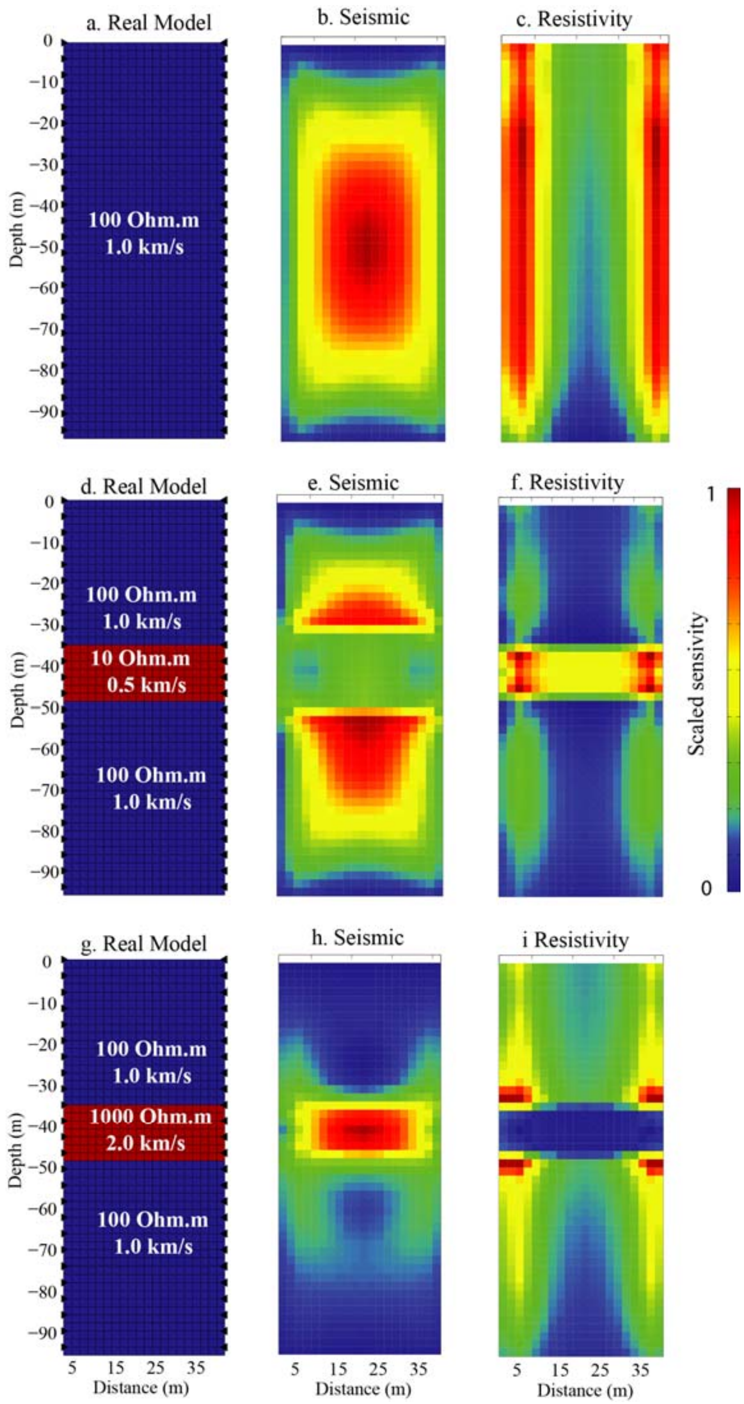

Figure 1. Sensitivity analysis for DC-resistivity and seismic velocities data. Each method shows different sensitivities in different areas of the space comprised between the two wells. The upper boundary is considered to be the air/ground interface.

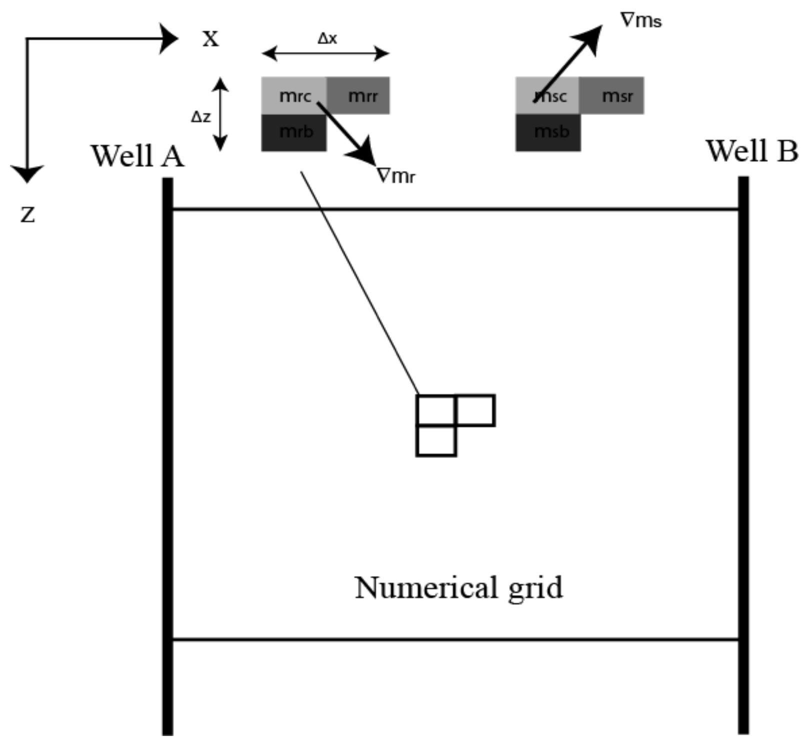

Figure 2. A 2.5 D grid used to model the resistivity and velocity of subsurface (*y* corresponds to the strike direction). The cross-gradient is defined with a three cell grid, at each position, following the approach developed by Gallardo and Meju (2003, 2004).

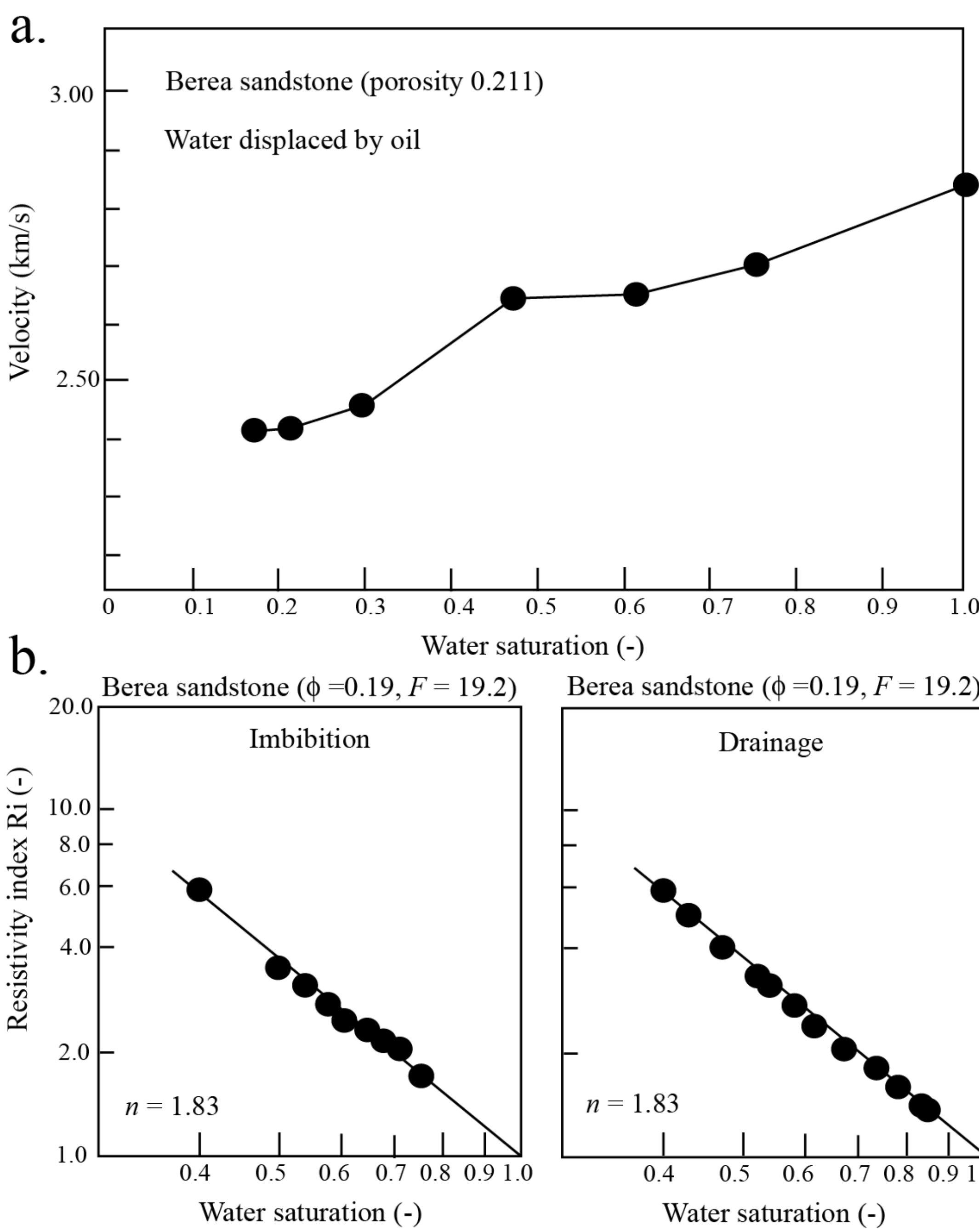

Figure 3. Influence of water saturation on seismic P-wave velocity and resistivity index (resistivity at a given saturation divided by the resistivity at saturation in the water phase). **a.** P-wave velocity (data from Wyllie et al., 1956). **b.** Resistivity index ($Ri = \sigma(s_w\!=\!1)/\sigma(s_w) \approx s_w^{-n}$; data from Jun-Zhi and Lile, 1990).

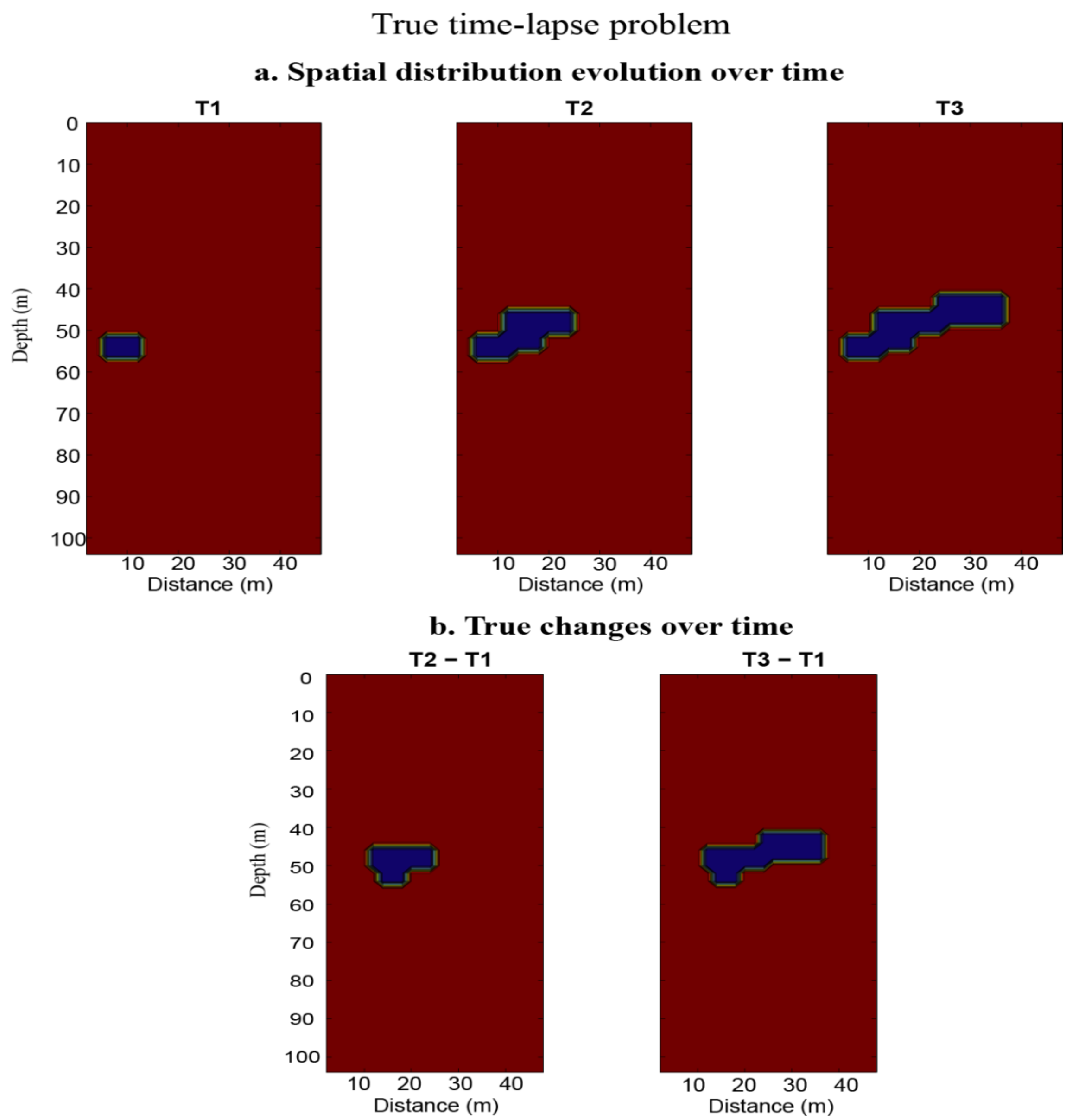

Figure 4. A benchmark of the joint inversion scheme. **a.** Evolution of a body of resistivity 100 Ohm m and velocity 2 km/s moving inside an homogeneous earth with a background resistivity of 10 Ohm m and a background velocity of 1 km/s. **b.** Differences between the three snapshots (T2 - T1) and (T3-T1).

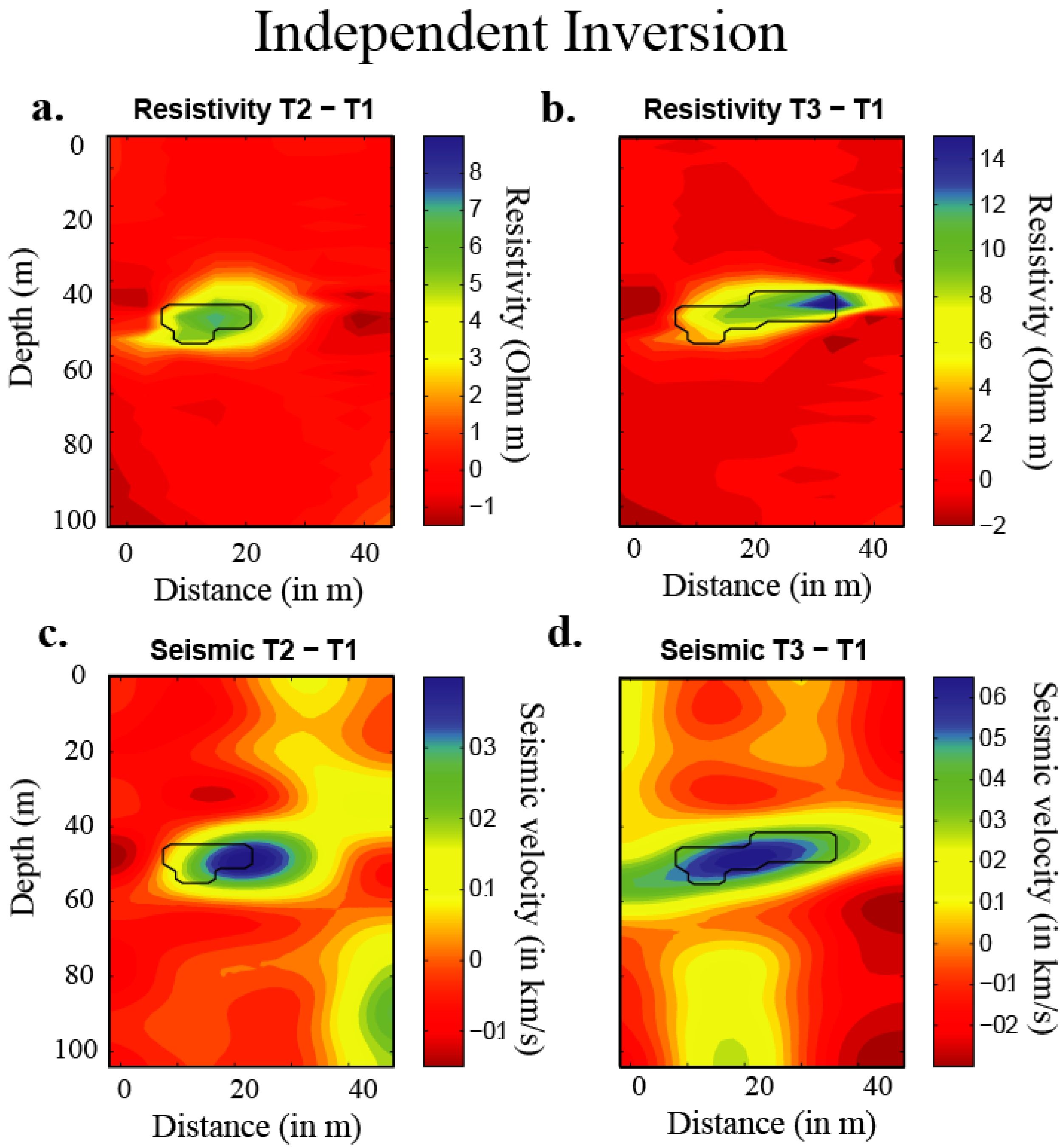

Figure 5. Independent inversion. **a.** and **b.** Independent inversion of the resistivity and display of the resistivity changes between time T2 and time T1 (a) and between time T3 and time T2 (b) at iteration 5. **c.** and **d.** Same For the seismic data. The thin black line denotes the true position of the change (see Figure 4).

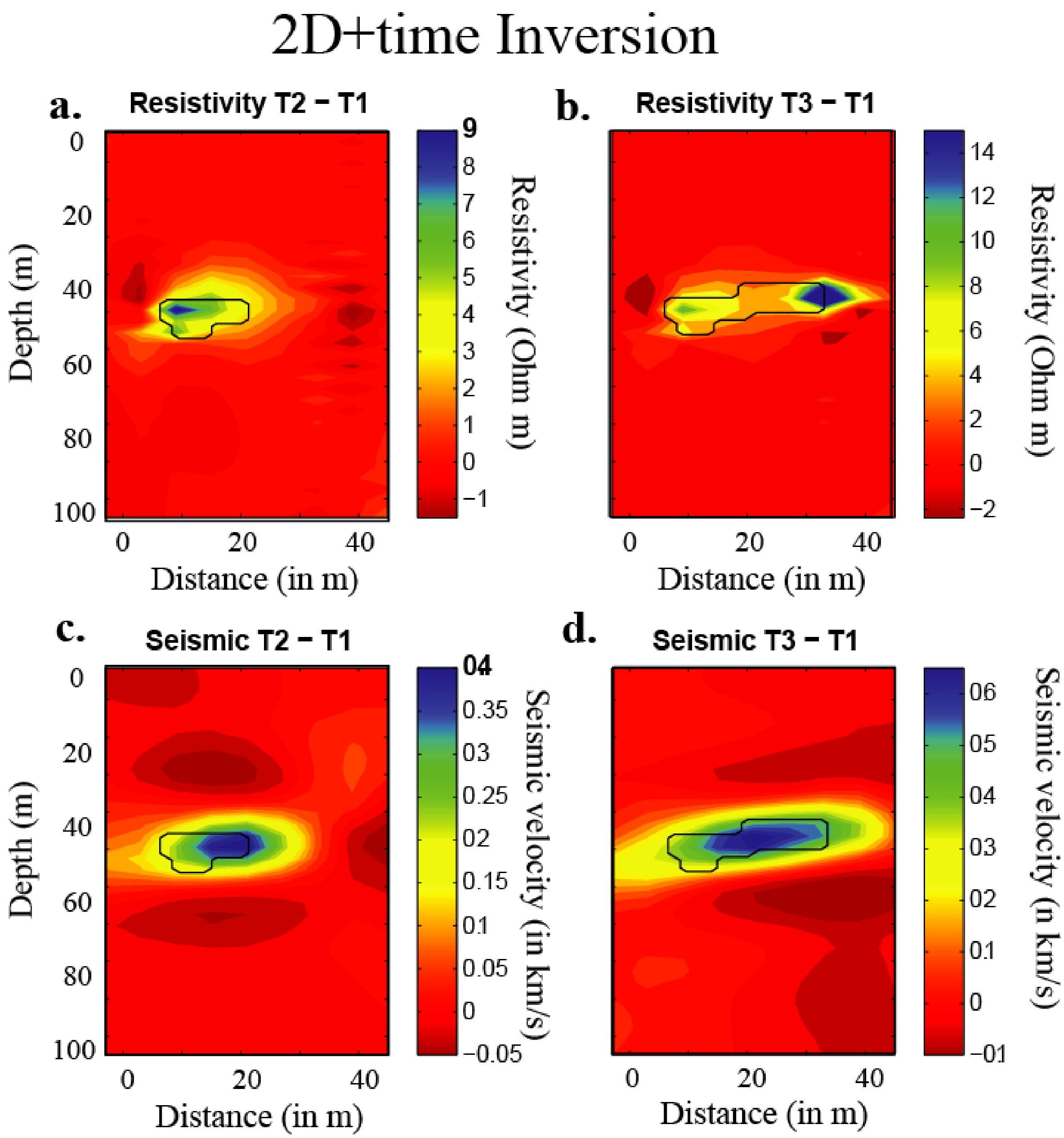

Figure 6. Independent time-lapse inversion. **a.** and **b.** Independent time-lapse inversion of the resistivity and display of the resistivity changes between time T2 and time T1 (a) and between time T3 and time T2 (b) at iteration 5. **c.** and **d.** Same For the seismic data. The thin black line denotes the true position of the change (see Figure 4).

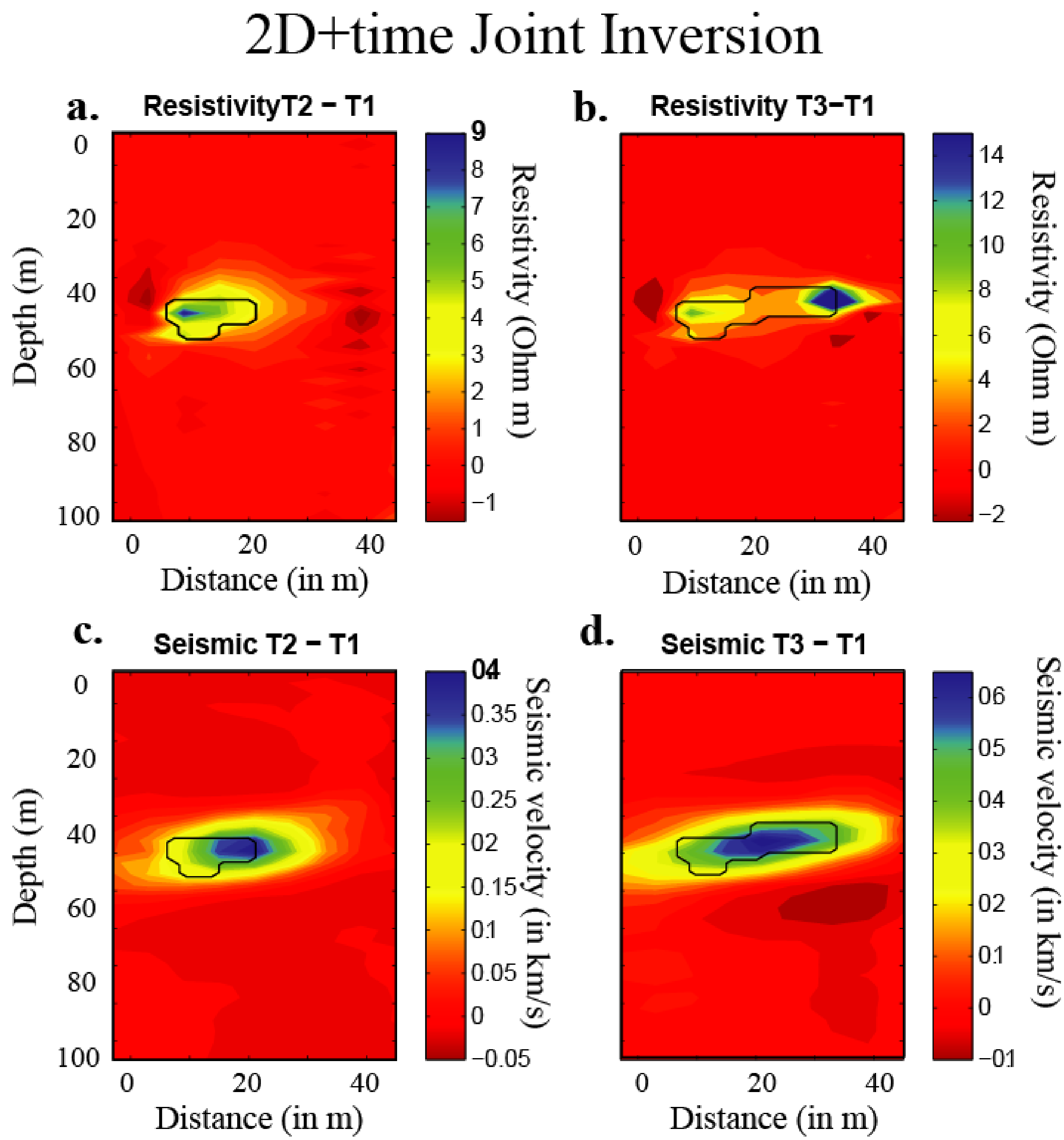

Figure 7. Joint time-lapse inversion. **a.** and **b.** Time-lapse joint inversion of the resistivity and seismic data and display of the resistivity changes between time T2 and time T1 (a) and between time T3 and time T2 (b) at iteration 5. **c.** and **d.** Same for the seismic data. The thin black line denotes the true position of the change (see Figure 4).

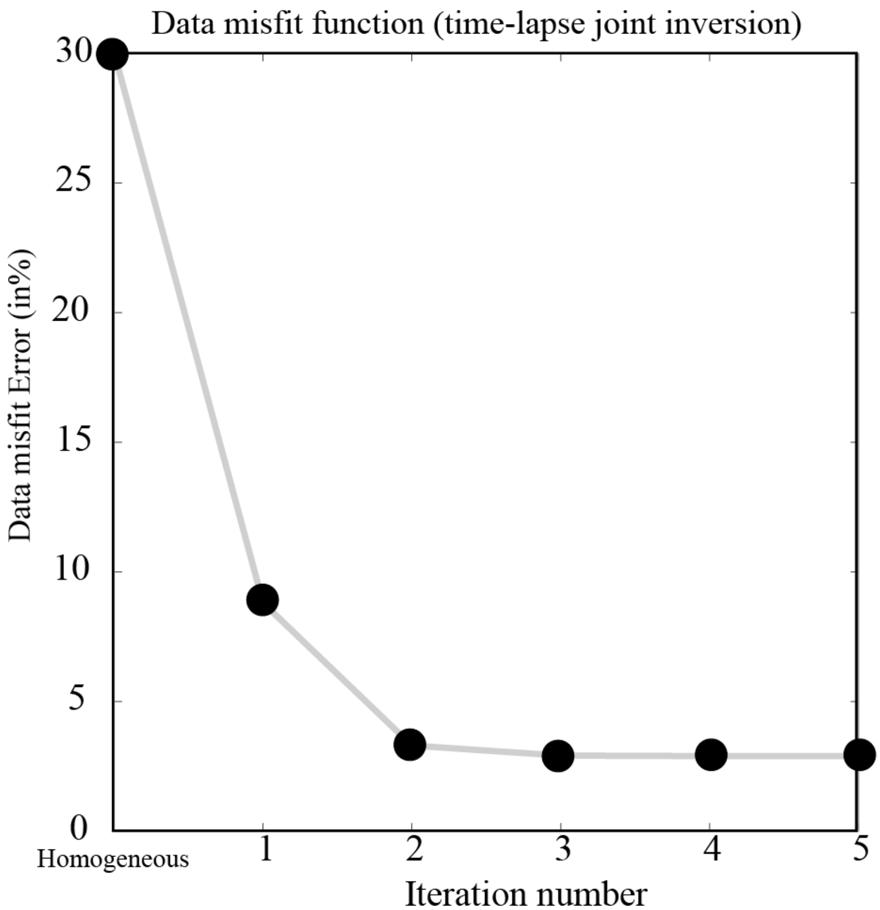

Figure 8. Evolution of the data misfit error with the number of iteration for the joint time-lapse inversion problem (the inversion is started with a homogeneous model distribution).

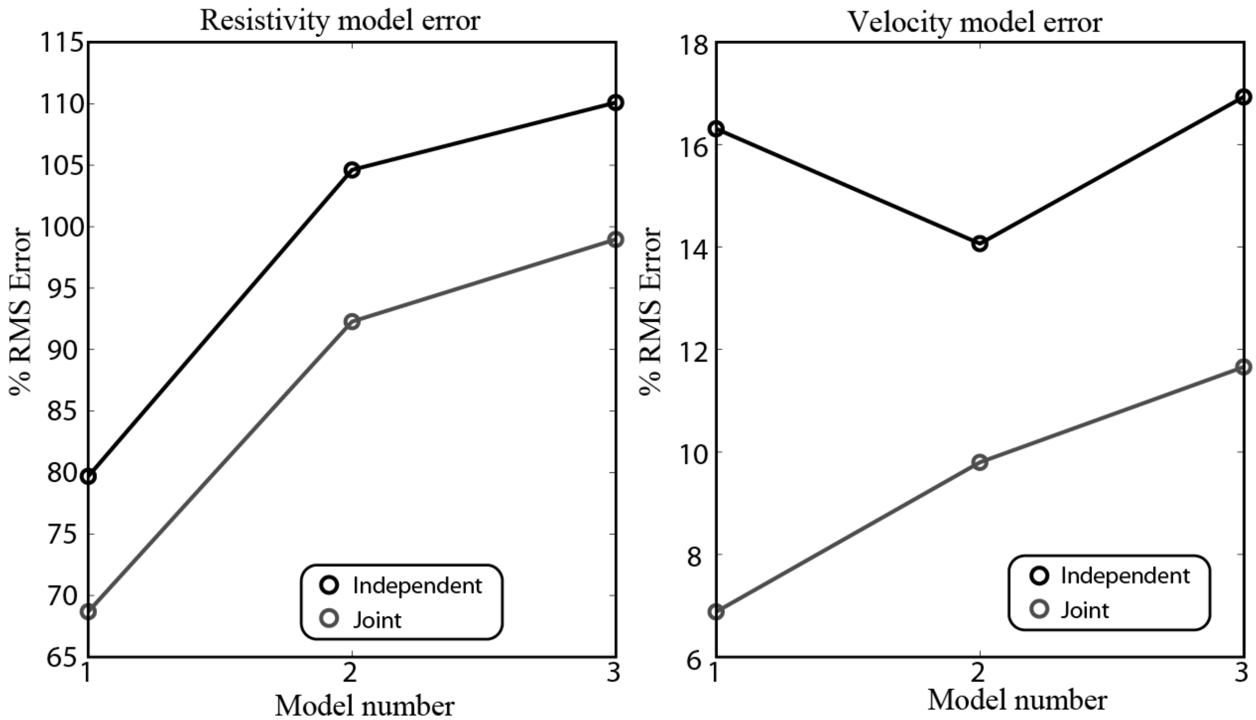

Figure 9. Time steps "model %RMS error" for the resistivity (left) and velocities (right) when using independent inversion (blue line) and the joint time-lapse algorithm (red line). In all time step models (T1, T2, and T3), the model RMS error is significant lower for the time-lapse joint inversion approach. This means that the time-lapse joint inversion is better reproducing the true model changes.

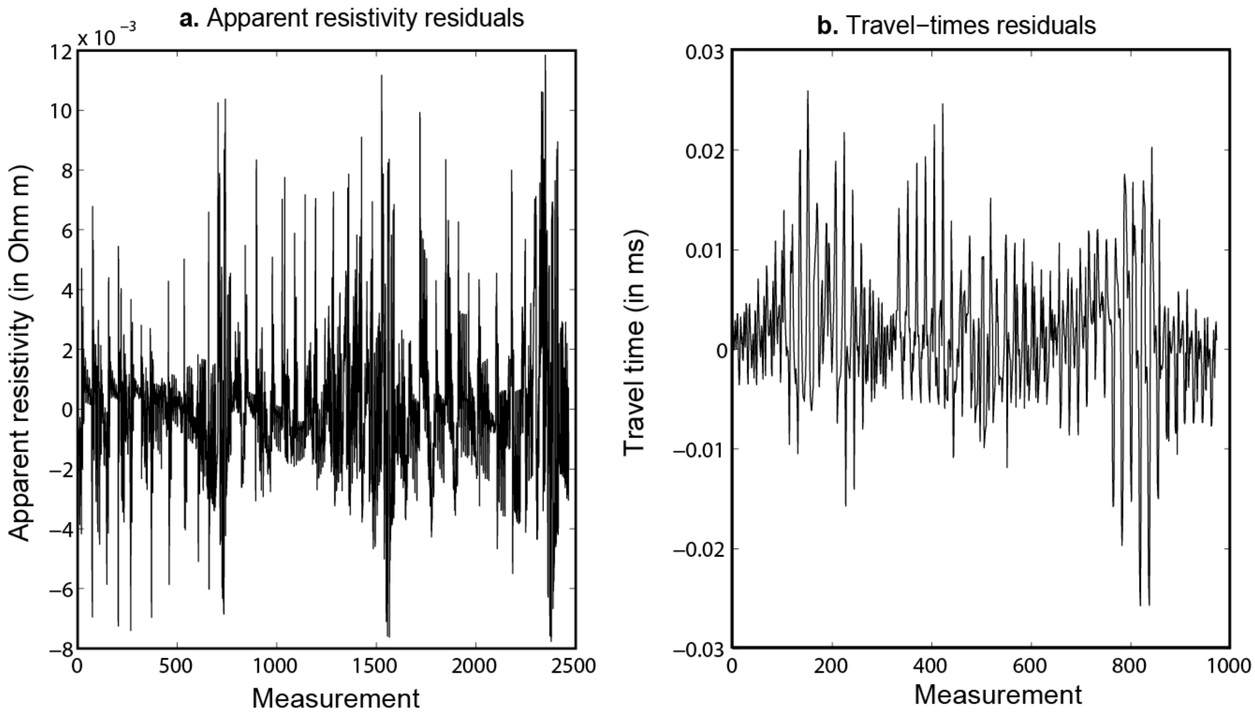

Figure 10. Data residuals for apparent resistivities (left) and travel time (right), for the synthetic model shown on Figure 4.

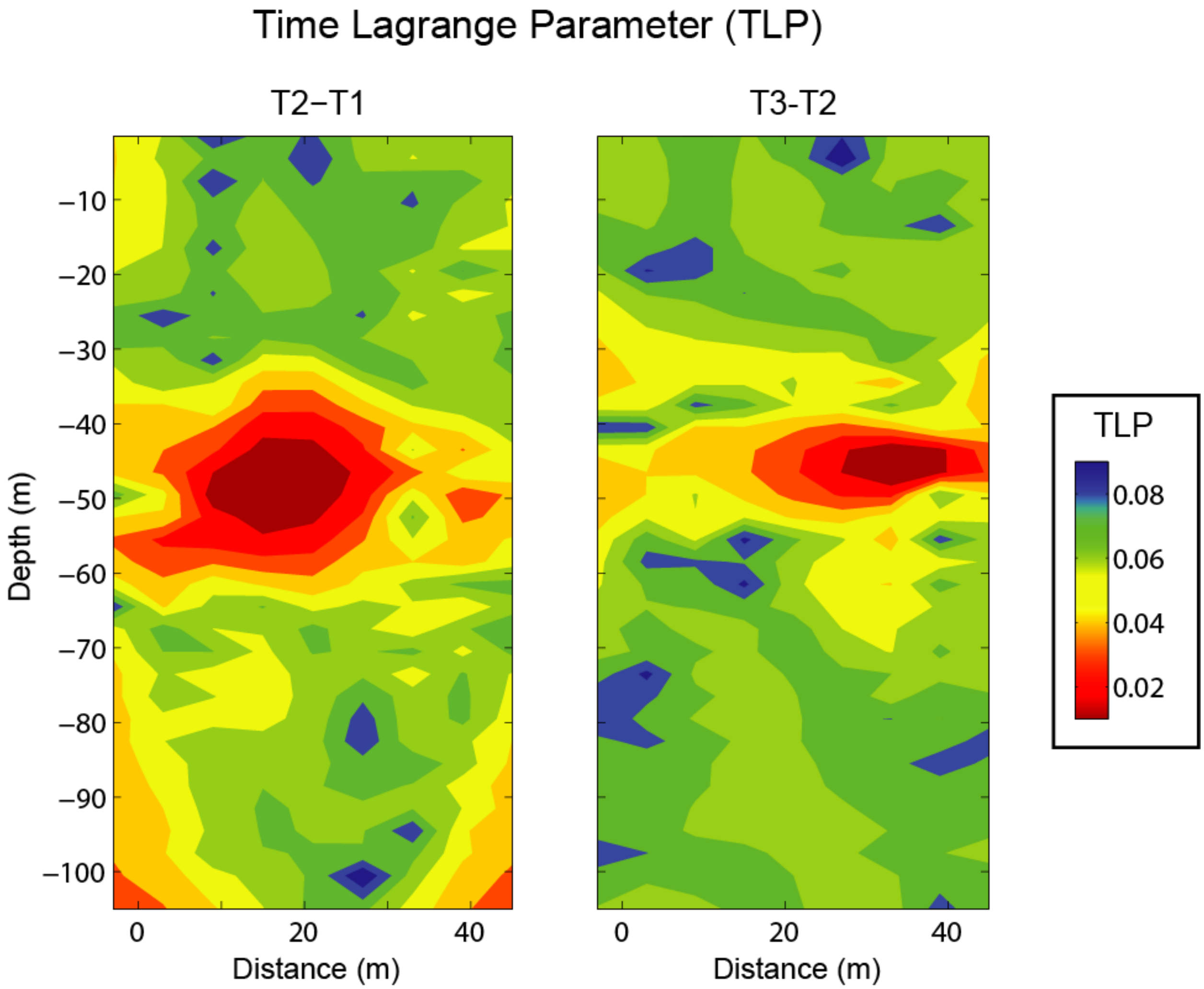

Figure 11. Distribution of the time-related Lagrange parameter. Low values of the Lagrange parameter indicate areas where time-related changes are expected.

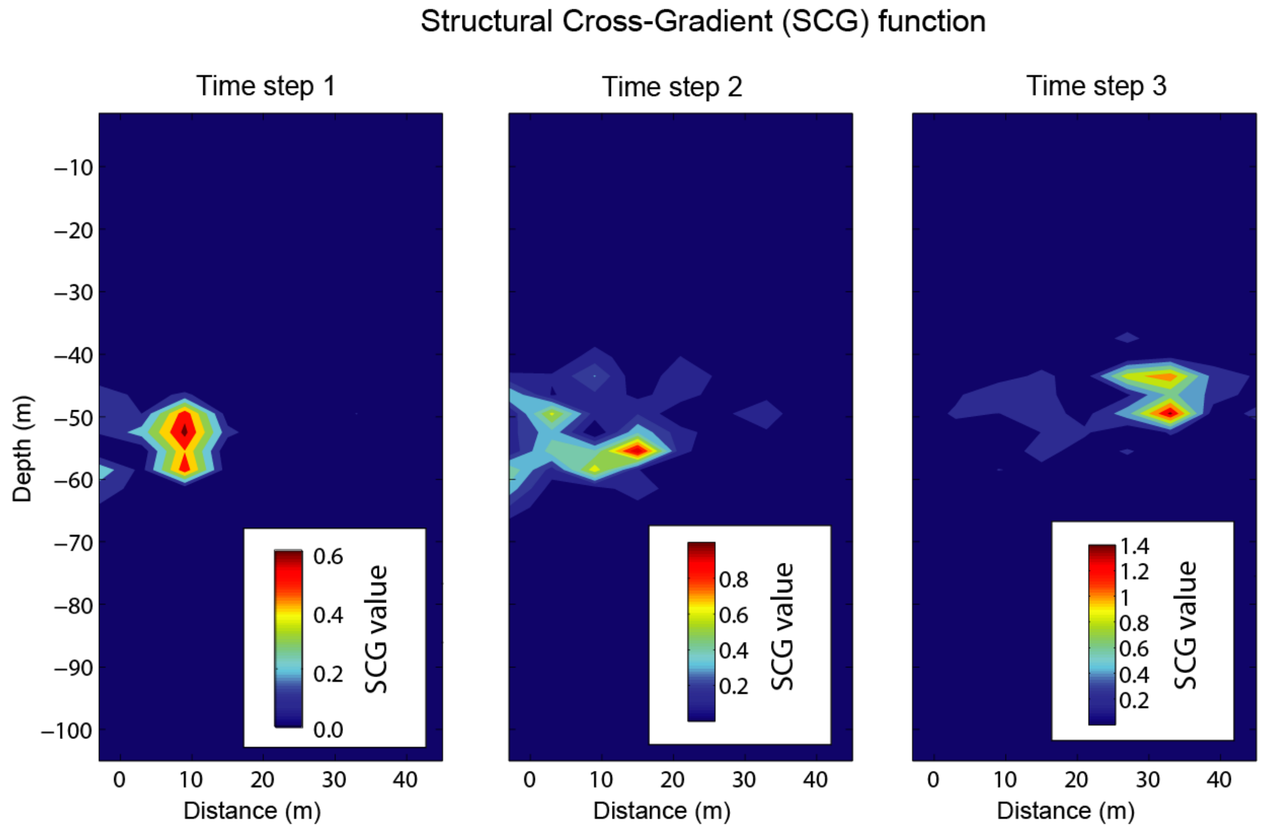

Figure 12. The cross-gradient function for the synthetic model. Large values indicate areas with high structural similarity between the resistivity and seismic model, which are expected at the boundary of the piece-wise constant models shown in Figure 4. Note that the synthetic model (see Figure 4) satisfies to the cross-gradient constraint.

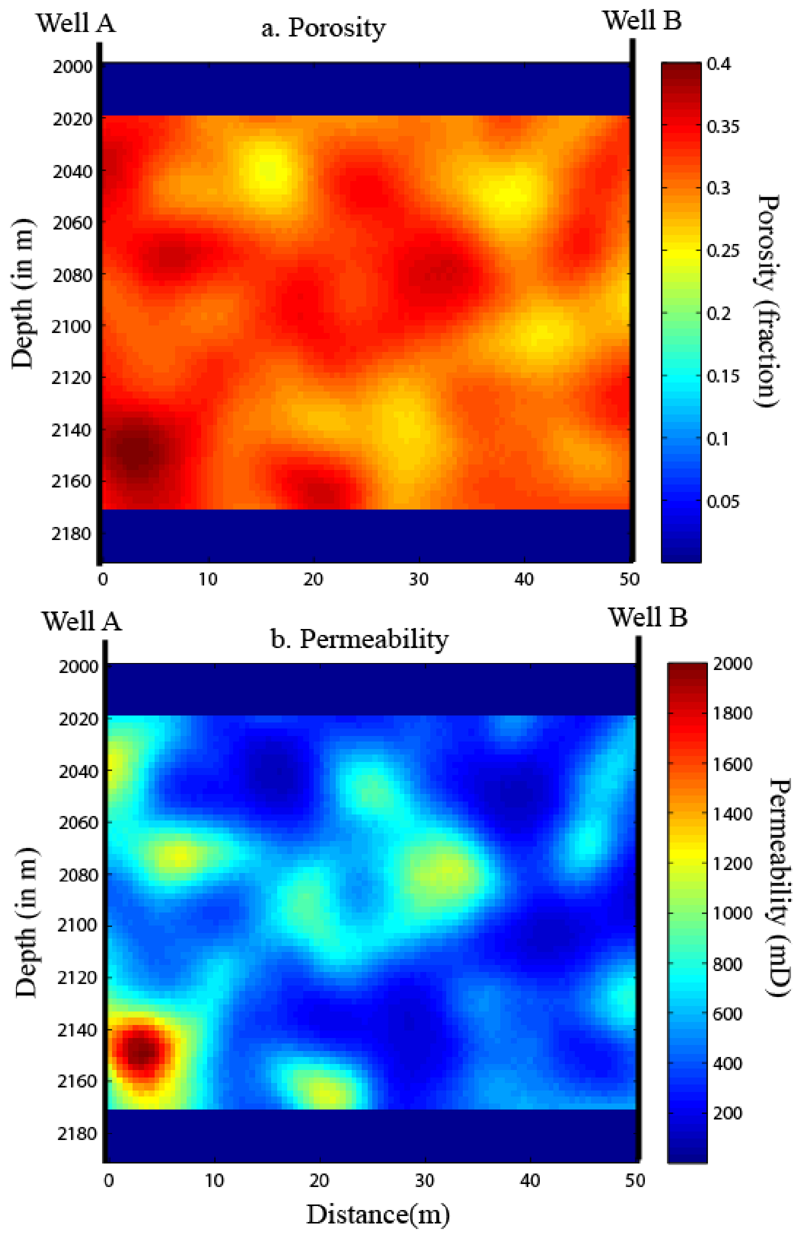

Figure 13. Porosity and permeability fields of a sandstone reservoir between two wells for the flood simulation numerical test.

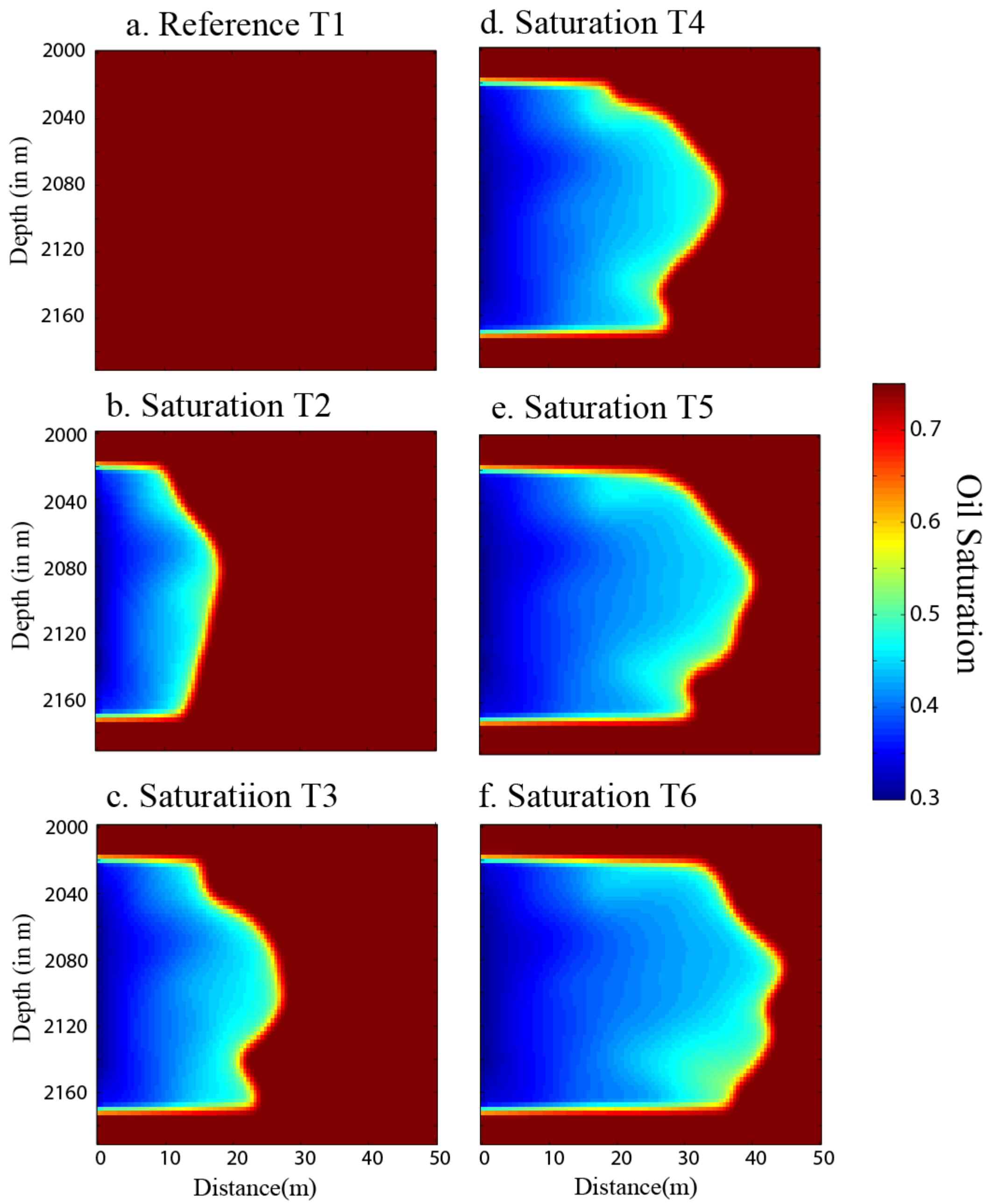

Figure 14. Six snapshots showing the evolution of the oil saturation over time in a 150 m-thick oil reservoir. The initial oil saturation in the reservoir is 0.75. Oil is considered to be the non-wetting phase.

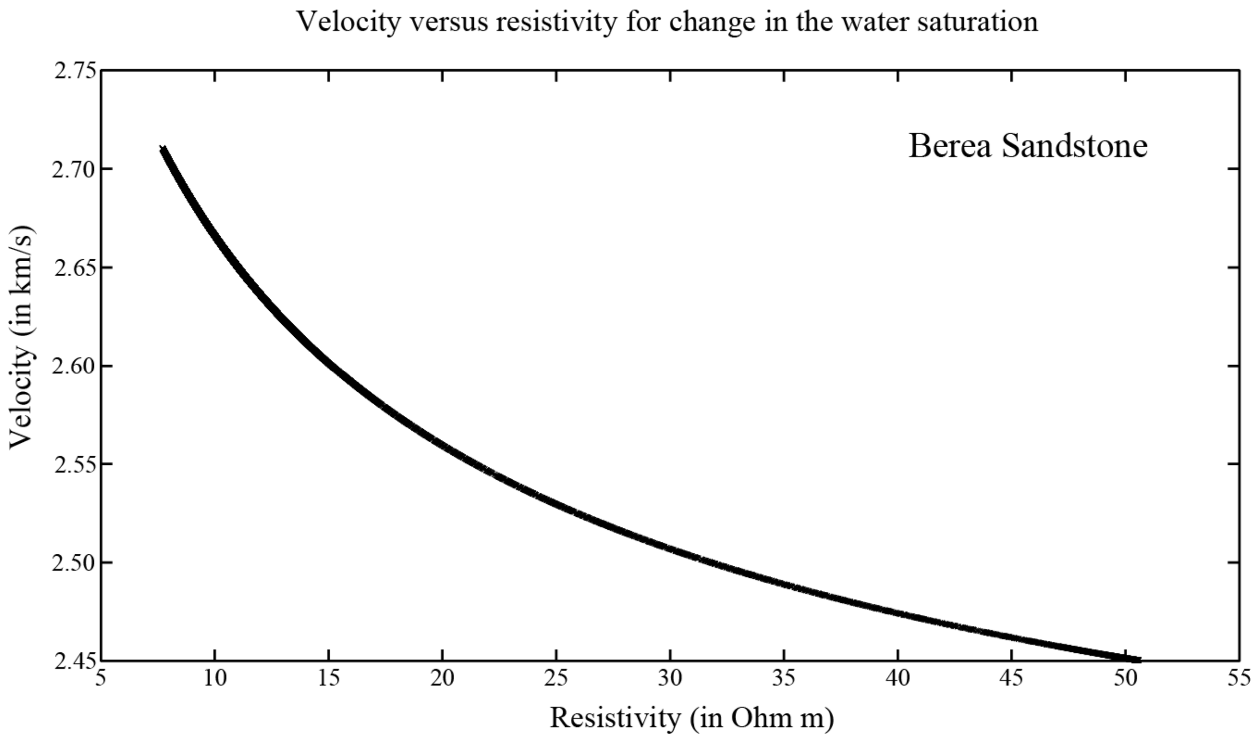

Figure 15. The relationship between resistivity and velocity for changes in the water saturation. This relationship is determined from the data shown in Figure 3.

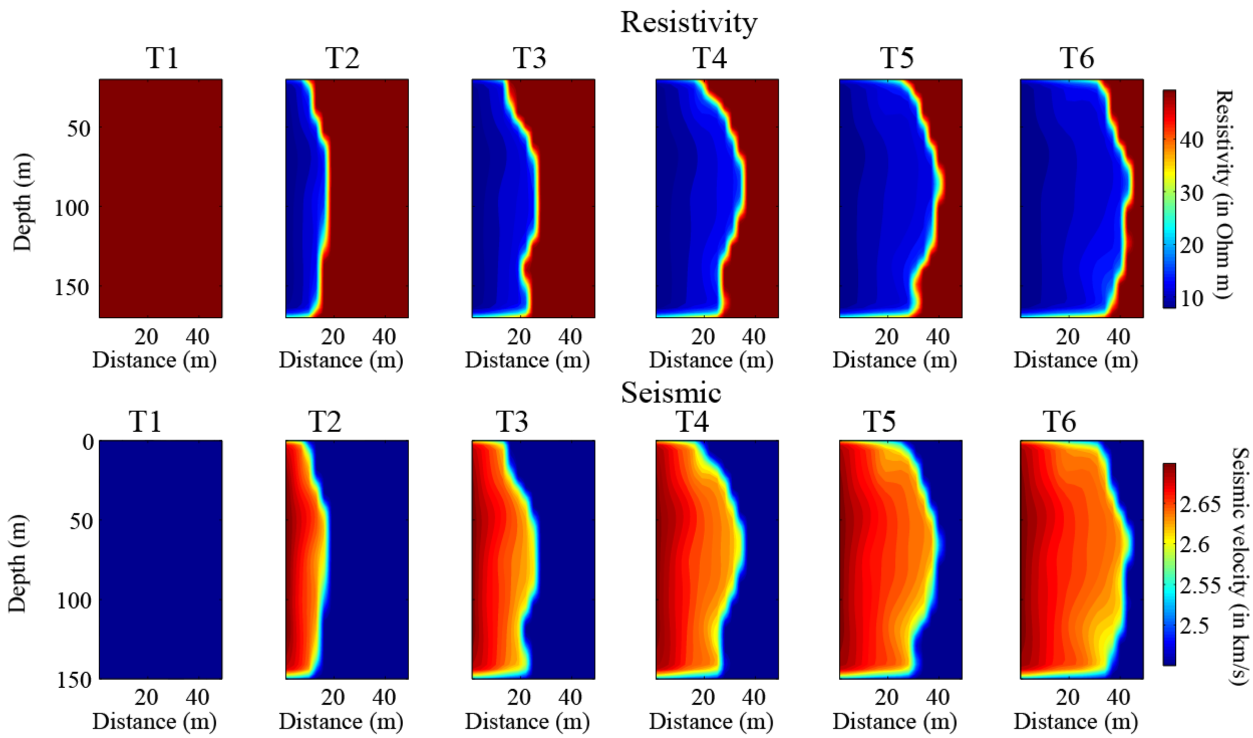

Figure 16. Simulated 6 time-step resistivity and velocity model, using data from Figure 3. T1 to T6 corresponds to the six snapshots shown in Figure 14.

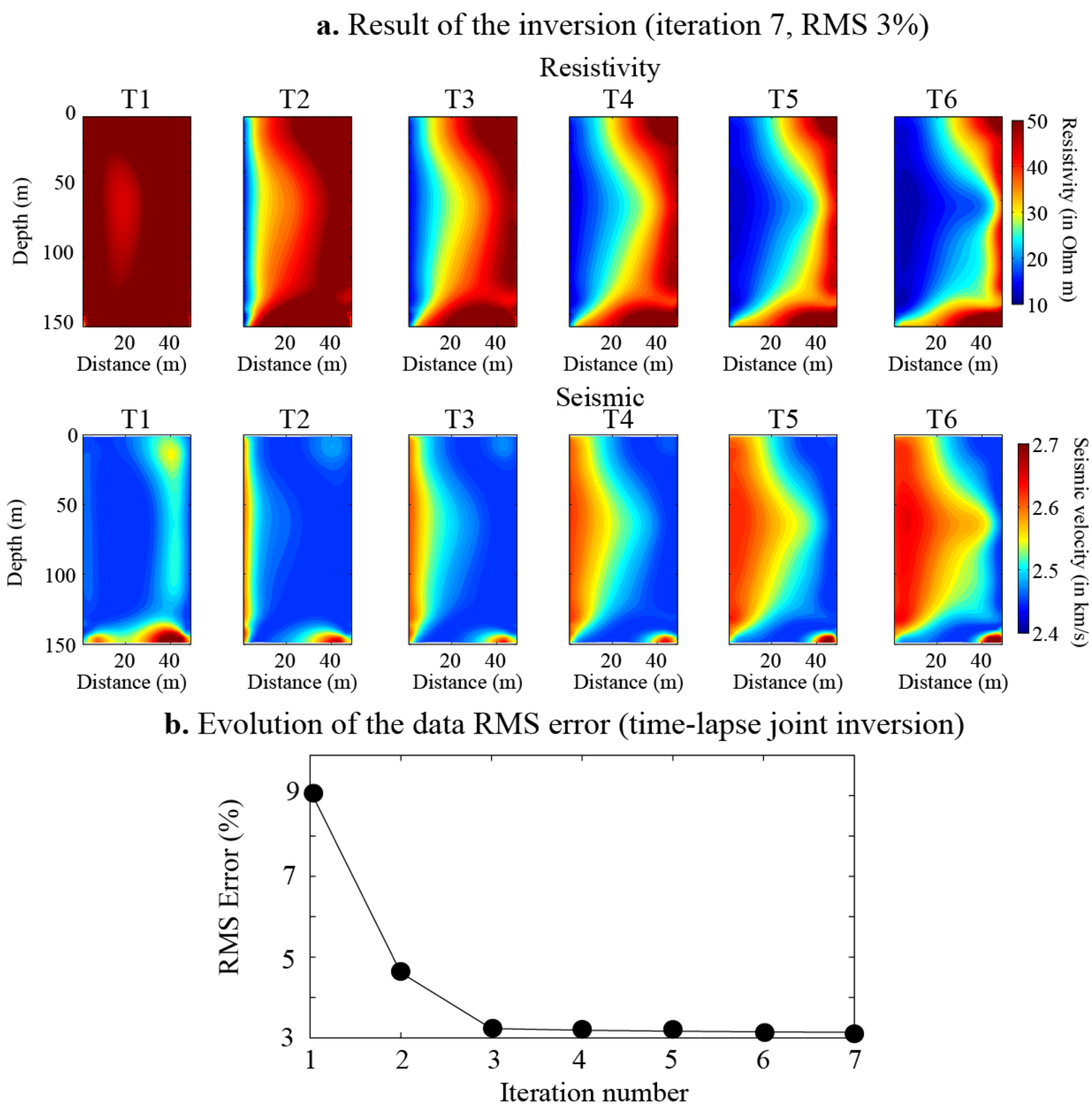

Figure 17. The inverted time-lapse resistivity and velocity models using the CP-based approach. The models T1 to T6 corresponds to the six snapshots shown in Figure 14.

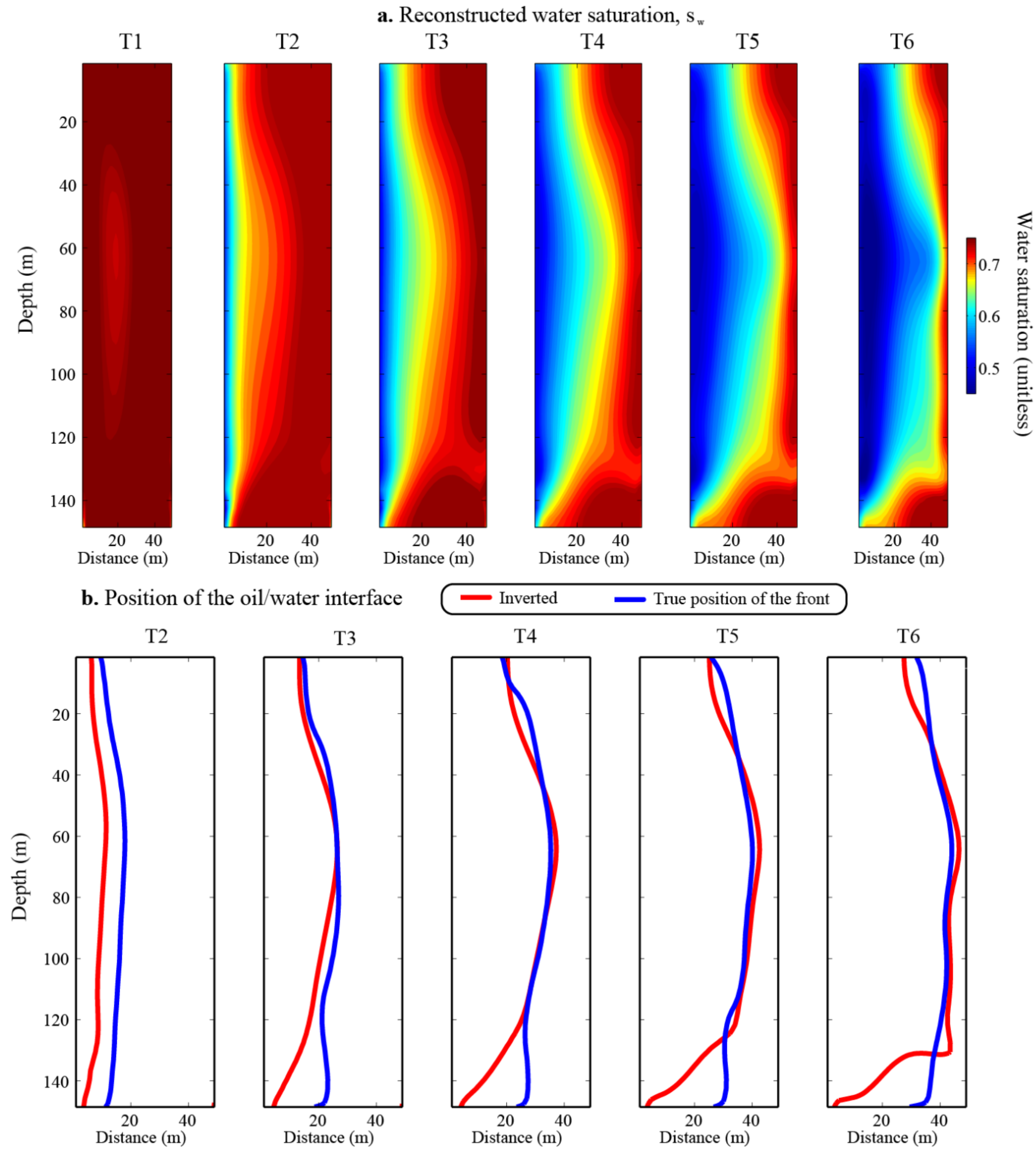

Figure 18. Position of the water front. **a.** Reconstruction of the saturation from the inverted resistivity. **b.** Reconstructed and true positions of the oil/water front moving inside the reservoir.